

**Methods for Reducing the Capital Costs of Electrolyzers for Hydrogen Generation**

by

Jesse Hudkins

B.S., Yale University, 2013

A THESIS SUBMITTED IN PARTIAL FULFILLMENT OF  
THE REQUIREMENTS FOR THE DEGREE OF

MASTER OF APPLIED SCIENCE

in

The Faculty of Graduate and Postdoctoral Studies  
(Chemical and Biological Engineering)

THE UNIVERSITY OF BRITISH COLUMBIA  
(Vancouver)

August 2016

© Jesse Hudkins, 2016

## Abstract

Amorphous phases of metal oxide thin films are of interest to the Berlinguette group because they mediate the oxygen evolution reaction more efficiently than crystalline phases of the same compositions. One goal of this thesis is to develop a technique to implement amorphous metal oxide thin films in a membrane electrode assembly (MEA) by depositing these highly active thin films on solid polymer electrolyte membranes. Chapter 2 outlines the implementation of amorphous iridium oxide ( $\alpha$ -IrO<sub>x</sub>) into a catalyst-coated membrane (CCM) to study amorphous thin film electrocatalysts in MEAs. Current densities of 10 mA cm<sup>-2</sup> were reached at relatively low overpotentials (~ 400 mV) for amorphous CCMs produced using the decal transfer method. This electrochemical response compares closely to that of amorphous iridium electrodeposited on conductive glass (10 mA cm<sup>-2</sup> at  $\eta$  = 430 mV). The second goal of this thesis is to lower the capital costs of alkaline electrolyzer units by using plastic as a surrogate for metal in field-flow plates. This achievement was demonstrated by electroplating nickel onto 3D-printed plastic flow-field plates. The test cells containing these metal-coated plastic components matched the performance of conventional metal components, despite containing 60-fold less metal. Chapter 4 summarizes this work and offers future directions of the research conducted for this thesis.

## **Preface**

The work done in this thesis was done under the supervision of Dr. Curtis P. Berlinguette.

Chapter 2 is based on my unpublished work conducted in the Berlinguette Laboratory at UBC. The identification and design of this research was developed with the guidance of Dr. Curtis P. Berlinguette. I performed all sample preparation, spectroscopic experiments, and electrochemical experiments and analyzed the data. Kevan Dettelbach performed X-ray diffraction experiments.

Chapter 3 is based on work conducted in the Berlinguette Laboratory at UBC by myself and Danika Wheeler. I was responsible for the designed of the original 3D flow-field, sample preparation, and electrochemistry experiments. Danika Wheeler was responsible for the 3D-printing and 3D-printer construction and maintenance. Danika identified and sourced all carbon-infused plastic used in the development of the plastic electrolyzer. Plastic electrolyzer design iterations and electroplating were performed in collaboration with Danika Wheeler.

I prepared the initial and final drafts of this thesis, with revisions by Dr. Curtis P. Berlinguette.

## Table of Contents

<b>Abstract.....</b>	<b>ii</b>
<b>Preface .....</b>	<b>iii</b>
<b>Table of Contents .....</b>	<b>iv</b>
<b>List of Tables.....</b>	<b>viii</b>
<b>List of Figures .....</b>	<b>ix</b>
<b>List of Abbreviations, Symbols and Nomenclature .....</b>	<b>xii</b>
<b>Acknowledgements .....</b>	<b>xvi</b>
<b>Dedication .....</b>	<b>xvii</b>
<b>Chapter 1: Introduction .....</b>	<b>1</b>
<b>1.1 Renewable Energy Storage .....</b>	<b>1</b>
<b>1.2 Electrolytic Water-Splitting Thermodynamics .....</b>	<b>2</b>
<b>1.3 Electrolyzer Technologies .....</b>	<b>5</b>
1.3.1 Alkaline Electrolyzers.....	7
1.3.2 Proton Exchange Membrane Electrolyzers .....	7
1.3.3 Anion Exchange Membrane Electrolyzers .....	12
<b>Chapter 2: Integrating Amorphous Iridium Oxide into Membrane Electrode Assemblies.....</b>	<b>14</b>
<b>2.1 Introduction .....</b>	<b>14</b>



<b>2.2</b>	<b>Results .....</b>	<b>16</b>
2.2.1	Decal Transfer Method.....	16
2.2.2	Physical Characterization of Amorphous Catalyst-Coated Membranes.....	19
2.2.3	Effect of CCM Modification on the Ionic Conductivity of Nafion .....	20
2.2.4	Electrochemical Characterization of Amorphous Catalyst-Coated Membranes .....	22
<b>2.3</b>	<b>Summary.....</b>	<b>24</b>
<b>2.4</b>	<b>Methods.....</b>	<b>25</b>
2.4.1	Materials .....	25
2.4.2	Sample Preparation .....	25
2.4.3	Physical Methods .....	26
<b>Chapter 3: Electroplating Enables 3D-Printed Components Tailored for Water Electrolysis ...</b>		<b>28</b>
<b>3.1</b>	<b>Introduction .....</b>	<b>28</b>
<b>3.2</b>	<b>Results .....</b>	<b>33</b>
3.2.1	Electroplating 3D-Printed Plastic.....	33
3.2.2	3D-Printed Plastic Flow-Field Plates .....	36
3.2.3	Electrocatalysis with Plastic Flow-Field Plates.....	38
<b>3.3</b>	<b>Summary.....</b>	<b>45</b>
<b>3.4</b>	<b>Methods.....</b>	<b>46</b>
3.4.1	Materials .....	46
3.4.2	3D-printing .....	46
3.4.3	Electrode Preparation and Ni Electroplating .....	47

3.4.4	MEA Preparation .....	48
3.4.5	Physical Methods .....	49
3.4.6	Flow-Plate Techno-Economic Analysis .....	50
<b>Chapter 4: Conclusion .....</b>		<b>53</b>
<b>4.1</b>	<b>Conclusion.....</b>	<b>53</b>
4.1.1	Amorphous Catalyst Coated Membranes .....	53
4.1.2	Nickel-plated, 3D-printed Plastic Electrolyzer Components.....	54
<b>4.2</b>	<b>Future Directions.....</b>	<b>55</b>
4.2.1	Amorphous Catalyst-coated Membranes.....	55
4.2.2	Electroplating on Commercial-Sized Electrolyzer Flow-Field Plates.....	55
<b>References.....</b>		<b>57</b>
<b>Appendices.....</b>		<b>63</b>
<b>Appendix A</b> Supplemental photographs for Chapter 2. ....		<b>63</b>
A.1	Teflon substrate before and after decal transfer.....	63
A.2	Cell setup for electrochemical impedance studies on the through-plane ion conductivity of modified Nafion membranes .....	63
A.3	Cell setup for electrochemical experiments conducted on amorphous iridium coated membranes. ....	64
<b>Appendix B</b> Supplemental photographs for Chapter 3. ....		<b>64</b>
B.1	Cell setup for 3-electrode studies on 3D-printed planar electrodes.....	64

B.2	Plastic electrolyzer cell setup. ....	65
-----	---------------------------------------	----

## List of Tables

<b>Table 2.1</b>	Temperatures and pressures tested in decal transfer study of $\alpha$ -IrO <sub>x</sub> /Nafion.....	19
<b>Table 2.2</b>	OER activities of $\alpha$ -IrO <sub>x</sub> films.....	24
<b>Table 3.1</b>	Normalized mass and raw materials cost of two common electrolyzer bipolar plates	31
<b>Table 3.2</b>	Volumetric resistivity of conductive 3D-printing filaments. ....	34
<b>Table 3.3</b>	Relative prices and densities of flow-field plate materials. ....	52
<b>Table 3.4</b>	Techno-economic analysis of electrolyzer bipolar plates .....	52

## List of Figures

**Figure 1.1** Cross-section cartoons of the different electrolyzer technologies discussed in this thesis. (A) Alkaline electrolyzer cells contain two electrodes immersed in 20-30% KOH that are separated by a separator membrane that are generally made of nickel oxide, asbestos, or polymers. Individual cells are separated by bipolar plates made of nickel or stainless steel in an electrolyzer stack configuration. (B) PEM electrolyzers contain flow-field plates that facilitate fluid and gas transport in the devices and are generally made of titanium. These flow-field plates sandwich the MEA that is generally comprised of titanium gas diffusion electrodes, platinum group metal catalyst layers, and a PEM membrane. Individual cells are separated by the flow-field plates in the electrolyzer stack configuration. (C) AEM electrolyzers contain flow-field that facilitate fluid and gas transport in the devices and are made of nickel or stainless steel. These flow-field plates sandwich the MEA that is generally comprised of nickel or stainless steel gas diffusion electrodes, first-row transition metal oxide catalyst layers, and an AEM membrane. Individual cells are separated by the flow-field plates in the AEM electrolyzer stack configuration. .... 6

**Figure 1.2** Schematic of (A) catalyst-coated substrate (CCS) and (B) catalyst-coated membrane (CCM). .... 10

**Figure 2.1** (A) Precursor  $[\text{Ir}(\text{acac})_3]$  spray-coated onto a Teflon substrate. (B) UVDD of sprayed-coated  $\text{Ir}(\text{acac})_3$  on a Teflon sheet to produce a thin film of  $\alpha\text{-IrO}_x$ . (C) Decal transfer using a hot press at variable temperatures and pressures. (D) Teflon decal substrate peeled from Nafion to reveal the final CCM. See Appendix for photos. .... 16

**Figure 2.2** FTIR spectra recorded on blank Teflon decal transfer substrate (*black*),  $\text{Ir}(\text{acac})_3$ -coated Teflon substrate (*orange*),  $\alpha\text{-IrO}_x$ /Teflon film on Teflon substrate after 7 h of UV radiation (*blue*), and Teflon substrate after decal transfer (*grey*). Absorption bands are associated with the vibrational modes of (A) C-O bonds (*ca.*  $1500\text{ cm}^{-1}$ ) and (B) C-H bonds (*ca.*  $2800\text{ cm}^{-1}$ ) of the acetylacetone ligand and vibrational modes of O-H bonds (broad peak centered *ca.*  $3300\text{ cm}^{-1}$ ) of chemisorbed oxyhydroxide. .... 18

**Figure 2.3** Powder XRD data acquired on (A)  $\alpha\text{-IrO}_x$  CCM prepared by decal transfer at  $125^\circ\text{C}$  and 1000 psi (*blue*), and a blank Nafion membrane (*red*); and (B)  $\alpha\text{-IrO}_x$  coated glass (*blue*) that underwent hot-pressing conditions of  $125^\circ\text{C}$  and 1000 psi for 1 min, the same sample after being heated at  $500^\circ\text{C}$  for 1 h (*red*), and blank glass (*black*). Powder XRD pattern (*red lines*) for crystalline  $\text{IrO}_2$  (JCPDS 15-790) are shown for reference. .... 20

**Figure 2.4** (A) Nyquist plots of through-the-plane impedance responses of Nafion membranes as received (*black*), hot-pressed at 500 psi and  $125^\circ\text{C}$  and annealed at  $150^\circ\text{C}$  (*blue*), and hot-

pressed at 1000 psi and 125 °C and annealed at 150 °C (*red*). (B) Ohmic resistances of hot-pressed membranes determined by through-plane measurements..... 22

**Figure 2.5** Electrochemical behavior of CCMs that underwent decal transfer at 125 °C and 1000 psi for 1 min. (A) Cyclic voltammograms recorded ( $v = 10 \text{ mV s}^{-1}$ ) on *a*-IrO<sub>x</sub> film deposited on Nafion (*blue*) and blank Nafion (*black*). Inset: Chronopotentiometry recorded on *a*-IrO<sub>x</sub> film deposited on Nafion at a anodic current density of  $10 \text{ mA cm}^{-2}$ . (B) Reproducibility of overpotential needed to achieve  $10 \text{ mA cm}^{-2}$  recorded on *a*-IrO<sub>x</sub> films deposited on Nafion recorded during the cyclic voltammogram (CV) and chronopotentiometry experiments at 30 s and 2 h. Electrochemistry conditions: counter electrode = Pt mesh; reference electrode = Ag/AgCl, KCl (sat'd); cyclic voltammogram scan rate =  $10 \text{ mV s}^{-1}$ ; chronopotentiometry current density =  $10 \text{ mA/cm}^2$ ; electrolyte =  $0.5 \text{ M H}_2\text{SO}_{4(aq)}$ . ..... 23

**Figure 3.1** Electrolyzer test cell. (A) Schematic of an exploded flow-plate test cell used in this study. Each 3D-printed electrolyzer housing is made of non-conductive ABS plastic and accommodates the titanium busbars and 3D-printed flow-field plates that are separated by the MEA. The MEA consists of Ni foam gas diffusion layers hot pressed onto each side of a Zirfon™ Perl UTP hydroxide conducting membrane. (B) Drawings (top) and photographs of 3D-printed PLA flow-field plate before (middle) and after electroplating (bottom) with nickel. The single serpentine flow-field pattern was used for all electrochemical studies in this study.. 32

**Figure 3.2** Electroplating comparison on 3D-printed electrodes. Left: Reprapper Conductive ABS, Middle: MatterHackers Conductive ABS, Right: Proto-Pasta conductive PLA..... 34

**Figure 3.3** (A) First and tenth cyclic voltammogram cycles recorded ( $v = 10 \text{ mV s}^{-1}$ ) on planar Ni:PLA (*red*) and planar PLA (*orange*). Inset: Chronopotentiometry recorded on the planar Ni:PLA at a anodic current density of  $4 \text{ mA cm}^{-2}$ . (B) The cathodic charge passed over the first 10 cyclic voltammetry sweeps conducted on a planar Ni:PLA electrode. Electrochemistry conditions: counter electrode = nickel foam; reference electrode = Ag/AgCl, KCl (sat'd); electrolyte =  $1.0 \text{ M KOH (aq)}$ ; cyclic voltammogram scan rate =  $10 \text{ mV s}^{-1}$ . Data not corrected for uncompensated resistance. .... 35

**Figure 3.4** 3D-printed flow-field plates with three different flow-field patterns..... 36

**Figure 3.5** High-angle cross sectional SEM of an electroplated nickel layer on a PLA flow-field plate..... 38

**Figure 3.6** 3D-printed electrolyzer test cell performance. (A) Staircase voltammetry recorded on electrolyzer cells with flow-field plates made of bulk Nickel 200 alloy (*blue*), conductive PLA (*orange*), nickel electroplated PLA (*red with squares*), and nickel electroplated PLA after >100 h of electrolyzer operation (*red with circles*). (B) Chronopotentiometry recorded on

electrolyzer cells with flow-field plates made of bulk Nickel 200 (*blue*), carbon PLA (*orange*), and nickel electroplated PLA (*red*) at a held current density of  $100 \text{ mA cm}^{-2}$ . Electrochemistry conditions:  $1.0 \text{ M KOH}_{(aq)}$ ; staircase voltammogram sample width = 30 s; staircase voltammogram sample period = 50 s. Data not corrected for ohmic resistance..... 39

**Figure 3.7** Chronoamperometry recorded on electrolyzer cells with flow-field plates made of bulk Ni (*blue*), carbon PLA (*orange*), and nickel electroplated Ni:PLA (*red*). Electrochemistry conditions: applied potential = 2.0 V; electrolyte =  $1.0 \text{ M KOH}_{(aq)}$ ..... 41

**Figure 3.8** (A) First cyclic voltammogram cycle recorded on a Ni:PLA flow-field plate (*red*) and a Ni flow-field plate (*blue*) in a 3-electrode cell. (B) Cyclic voltammograms were measured in a non-Faradaic region of the voltammogram at the following scan rate: 0.05, 0.1, 0.2, and  $0.4 \text{ V/s}$ . All current is assumed to be due to capacitive charging. Electrochemistry conditions: counter electrode = nickel foam; reference electrode = Ag/AgCl, KCl (sat'd); electrolyte =  $1.0 \text{ M KOH}_{(aq)}$ ; cyclic voltammogram scan rate =  $10 \text{ mV s}^{-1}$ . Data not corrected for uncompensated resistance..... 42

**Figure 3.9** Alternating current electrochemical impedance spectroscopy (EIS) recorded on electrolyzers with different flow-field materials. (A) Nyquist plots of EIS recorded on electrolyzer cells with flow-field plates made of bulk Nickel 200 alloy (*blue*), conductive PLA (*orange*), nickel electroplated PLA (*red*). Solid lines indicate data recorded before electrolysis experiments, dashed lines indicate data recorded after 24 h testing. Three different examples of data recorded on Ni:PLA are shown. All EIS was recorded at open cell potential (OCP). (B) Ohmic cell resistances extrapolated from electrochemical impedance spectra recorded on electrolyzer cells with flow-field plates made of bulk Ni 200 alloy (*blue*), conductive PLA (*orange*), nickel electroplated Ni:PLA (*red*). ..... 43

**Figure 3.10** Elemental analysis of six different points on the central flow-field rib (fifth rib from top) using energy-dispersive x-ray spectroscopy. Representative EDS spectrum: x-axes = energy (keV); y-axes = intensity (counts). (A) Before electrolysis. (B) After 24 h chronoamperometry and 24 h chronopotentiometry. .... 44

**Figure 3.11** SEM image of an electroplated nickel layer on a PLA flow-field plate before and after 48 h of electrolysis..... 45

## List of Abbreviations, Symbols and Nomenclature

Symbol	Definition
3D	Three-dimensional
°C	Degrees Celsius
A	Ampere
$A$	Area
a.u.	Arbitrary units
ABS	Acrylonitrile butadiene styrene
aq	Aqueous
$a\text{-IrO}_x$	Amorphous iridium oxide
AEM	Anion exchange membrane
CL	Catalyst layer
CCM	Catalyst-coated membrane
CCS	Catalyst-coated substrate
cm	Centimeter
CO <sub>2</sub>	Carbon dioxide
CO <sub>3</sub> <sup>2-</sup>	Carbonate ion
dm	Decameter
e <sup>-</sup>	Electrons
$E^\circ$	Potential at standard conditions
$E_{cell}$	Measured cell potential
$E_{e,T}$	Equilibrium potential at temperature T



Eq.	Equation
$F$	Faraday's constant
GDL	Gas diffusion layer
h	Hour(s)
H <sub>2</sub>	Diatomic hydrogen
H <sub>2</sub> O	Water
HCO <sub>3</sub> <sup>-</sup>	Bicarbonate
HER	Hydrogen evolution reaction
$i$	Current
IR	Infrared
IrO <sub>2</sub>	Iridium dioxide
$j$	Current density
$l$	Length
M	Molar
MW	Megawatt
mA	Milliamps
MEA	Membrane electrode assembly
mg	Milligram
min	Minute(s)
mL	Milliliter
$n$	Number of electrons in the reaction
NASA	National Aeronautics and Space Administration

Ni	Nickel
NiMo	Nickel molybdenum alloy
NIR	Near-infrared radiation
NIRDD	Near-infrared-driven decomposition
nm	Nanometers
O <sub>2</sub>	Diatomic oxygen
OH <sup>-</sup>	Hydroxide ion
OER	Oxygen evolution reaction
PGM	Platinum group metal
PEM	Proton exchange membrane
PLA	Polylactic acid
Pt	Platinum
PTFE	Polytetrafluoroethylene
PV	Photovoltaic
$R_{\Omega}$	Ohmic resistance
RHE	Reversible hydrogen electrode
RuO <sub>2</sub>	Ruthenium dioxide
S	Siemens
s	Second(s)
SPE	Solid polymer electrolyte
STP	Standard temperature and pressure
$T$	Temperature

TW	Terawatt
UV	Ultraviolet radiation
UVDD	UV-driven decomposition
V	Volts
XRD	X-ray diffraction
$\Delta G$	Reaction Gibbs free energy
$\Delta H$	Reaction enthalpy
$\Delta S$	Reaction entropy
$\Omega$	Ohms
$\Omega$ cm	Ohm centimeters
$\eta$	Overpotential
$\lambda$	Wavelength
$\mu\text{m}$	Micrometers
$\rho$	Resistivity

## **Acknowledgements**

I would like to express appreciation to my supervisor Dr. Curtis P. Berlinguette. Your dedication to excellence contributed greatly to my growth as a student and researcher. I will be forever grateful for the opportunity to be a member of your research program.

Thank you to my defense committee members Dr. David Wilkinson and Dr. Elod Gyenge for their time and critical analysis of my work.

I would like to thank the many Berlinguette group members, past and present, with whom I've had the pleasure of working alongside. My lab mates, in no particular order, Valerie Chiykowski, Rebecca Sherbo, Kevan Dettelbach, Danika Wheeler, Danielle Salvatore, Cameron Kellett, Tengfei Li, Amber Blair, Molly Sung, Sarah Simon, Danika Wheeler, Ben MacLeod, Fraser Parlane, Kitty Chen, Ken Hu, Alicia Koo, Chaun Du, Dr. Brian Lam, Dr. Phil Schauer, Dr. Rodney Smith, Dr. Rebecca Smith, Dr. Vincent Wang, Dr. Bruno Peña Maceda and Dr. Jeffery He. These group members are not only wonderful scientists but also great people and have made every day spent in the lab enjoyable. I would like to give special thanks to Danika Wheeler and Kevan Dettelbach with whom I've worked very closely on much of the work presented in this thesis. I would also like to give special thanks to Dr. Rodney Smith for providing immense guidance and mentorship.

## Dedication

*I dedicated this thesis to my parents, Darren and Cindy.  
Your love and support made this humble achievement possible.*

## **Chapter 1: Introduction**

### **1.1 Renewable Energy Storage**

The rate of global energy consumption is predicted to reach 30 terawatts (TW) by 2050.<sup>1</sup> The geopolitical, environmental, and economic security for all global citizens will partly depend on meeting this energy demand. The challenge is to develop methods for meeting this energy demand while stabilizing carbon dioxide concentrations in the atmosphere. This challenge is exacerbated by the fact that carbon-neutral energy sources are difficult to scale. To produce 10 TW of nuclear power requires a power plant to be constructed every day for the next 50 years. The maximum total hydrological potential of the planet is only 4.6 TW, wind turbines can only offer 2 TW of electrical energy, and biomass is limited by the net efficiency ( $\sim 5.6\%$ ) of natural photosynthesis.<sup>2</sup> These carbon-neutral sources collectively fall short of providing the tens of terawatts needed to meet global energy demand.<sup>1</sup>

The only renewable energy source that can meet our future energy needs is the Sun. The Sun delivers 120,000 TW to the Earth, and thus by covering merely 0.16% of the land on Earth with 10% efficient solar conversion systems, 20 TW of energy can be captured.<sup>3,4</sup> Solar energy capture and use is complicated by the diurnal and meteorological fluctuations that effect solar insolation. This intermittence necessitates the implementation of a scalable solar energy storage mechanism that will provide energy to consumers when it is needed.<sup>1,5</sup>

The production of fuels from renewable energy sources for storage over a wide range of timescales is vital for the utilization of the large-scale renewable energy capture.<sup>1,5-9</sup> Hydrogen has been widely discussed as a central energy carrier for a renewable energy economy due to its

high gravimetric energy density ( $120 \text{ MJ kg}^{-1}$ ),<sup>1,5,6,10-17</sup> and it can be utilized electrochemically in a hydrogen fuel cell.<sup>10,18-25</sup> Hydrogen is also consumed in the production of other useful products, such as upgraded hydrocarbon fuels and ammonia production.<sup>18</sup> Electrolyzers are likely to play a key role in the future of renewable energy systems by serving to store renewable electricity as hydrogen fuels, an application that motivates the work in this thesis.

## 1.2 Electrolytic Water-Splitting Thermodynamics

The electrolysis of water involves two non-spontaneous half-cell reactions: the oxygen evolution reaction (OER; Eq. 1) at the anode; and the hydrogen evolution reaction (HER; Eq. 2) at the cathode.



The standard reduction potentials of the half-cell reactions and the standard overall cell potential ( $E^{\circ}$ ) are indicated. The relation of  $E^{\circ}$  at any temperature to the Gibbs free energy change ( $\Delta G^{\circ}$ ) is expressed by:

$$\Delta G^{\circ} = -nFE^{\circ} \quad (\text{Eq. 4})$$

where  $n$  is the number of electrons involved in the electrochemical reaction and  $F$  is Faraday's constant ( $9.65 \times 10^4 \text{ C mol}^{-1}$ ). Under non-standard conditions, the  $\Delta G$  at constant temperature ( $T$ ) is related to Gibbs free energy change at standard conditions at constant temperature ( $\Delta G^{\circ}_T$ ) by:

$$\Delta G_T = \Delta G^\circ_T + RT \ln K_r^* \quad (\text{Eq. 5})$$

where  $R$  is the ideal gas constant and  $K_r^*$  is the reaction quotient. The reaction quotient for the overall water-splitting reaction is expressed by:

$$K_r^* = \prod_j a_j^{s_j} = \frac{a_{H_2}^2 a_{O_2}}{a_{H_2O}^2} \quad (\text{Eq. 6})$$

where  $\prod$  is product notation;  $a_j$  is the activity of species  $j$ ; and  $s_j$  is the stoichiometric coefficient of species  $j$ .

Eq. 4, 5, and 6 can then be combined to give the Nernst equation:

$$E_{e,T} = E^\circ_T - \frac{RT}{nF} \ln \prod_j a_j^{s_j} \quad (\text{Eq. 7})$$

where  $E^\circ_T$  is the standard equilibrium potential at the temperature of the system and  $E_{e,T}$  is the non-standard equilibrium potential at the temperature of the system.

A temperature correction must also be applied to determine the cell potential at a temperature other than 25 °C. Pressure is assumed to constant in one of Maxwell's thermodynamic equations to incorporate this correction:

$$\frac{d\Delta G^\circ_T}{dT} = -\Delta S^\circ \quad (\text{Eq. 8})$$

where  $\Delta S^\circ$  is the standard entropy change of the reaction ( $\text{J mol}^{-1}$ ). Equation 4 can be substituted into equation 8, which is simplified assuming  $\Delta S^\circ$  is constant over this change of temperature:

$$\frac{\partial E^\circ_T}{\partial T} = \frac{\Delta S^\circ}{nF} \quad (\text{Eq. 9})$$

Determining the thermodynamic voltage of a cell under the prevailing experimental conditions by applying the Nernst equation and correcting for temperature is an important step in



understanding the voltage efficiency of an electrolyzer. An electrolyzer cell operating at 100 °C, for example, will have a significantly lower  $E^\circ$  ( $E^\circ_{373\text{ K}} = -1.166\text{ V}$ ) than a cell operating at 25 °C ( $E^\circ_{298\text{ K}} = -1.229\text{ V}$ ).

As electrical and ionic currents flow through the cell, the internal resistances of the cell generate extra heat in electrolysis cells that helps drive the water-splitting reaction forward. The total voltage, including the thermal energy, required to split water is equal to 1.481 V at standard conditions and 298.15 K (25 °C), which corresponds to the higher heating value of the product hydrogen ( $V_{\text{HHV}}$ ). It is therefore customary to use  $V_{\text{HHV}}$  when calculating the electrical-energy efficiency of an electrolyzer:

$$\text{efficiency} = \frac{V_{\text{HHV}}}{V_{\text{Obs}}(i)} \quad (\text{Eq. 10})$$

where,  $V_{\text{Obs}}(i)$  is the observed operating voltage at current  $i$ .

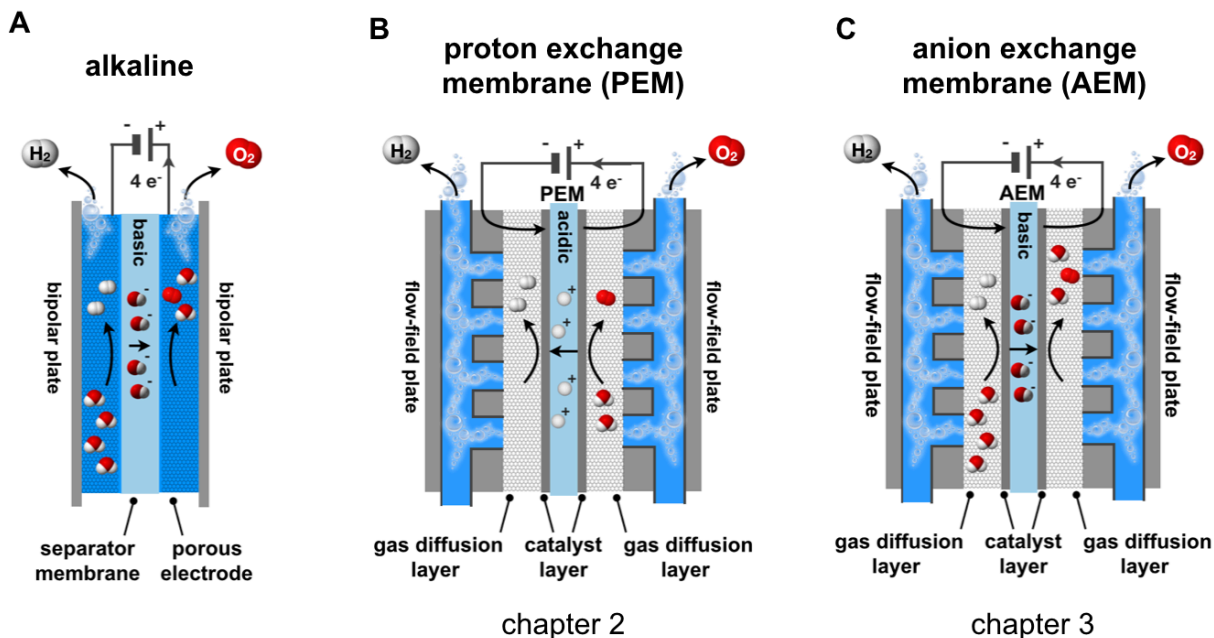
The efficiency of an electrolyzer is reduced at progressively higher current densities. Consequently, the focus of electrolyzer engineering is to reduce voltage inefficiencies where energy is lost in the form of heat.<sup>28</sup> These inefficiencies include overpotentials associated with the electron transfer kinetics and product and reactant diffusion at both the OER and HER electrodes and the ohmic resistance losses of the cell. The resistance through the conductive components of the electrolyzer, contact resistance at interfaces, and the resistance of ion transport in the electrolyte constitute the ohmic resistance in the cell ( $R_\Omega$ ). Design and materials considerations of conductive components, as well as the ionic conductivity of the electrolyte will also affect the efficiency of the cell by changing the overall ohmic resistance of the cell.

Overpotentials due to electron transfer kinetics and diffusion can be reduced by adding electrocatalysts and manipulating the hydrodynamics near the electrochemical reaction site, respectively.

The development of higher efficiency electrolyzers therefore requires more efficient electrocatalysts and new cell designs (e.g., reducing the ionic gap between electrodes).<sup>29,30</sup> This thesis will address these two goals in Chapters 2 and 3, respectively.

### **1.3 Electrolyzer Technologies**

There are two main types of low-temperature water electrolyzers: alkaline water electrolyzers; and proton exchange membrane (PEM) water electrolyzers (Fig. 1.1).<sup>29</sup> Each of these electrolyzers is distinct in terms of chemistry (e.g., alkaline versus acidic electrolyte), architecture, and components (e.g., porous separator diaphragm versus solid polymer electrolyte membrane). The anion exchange membrane (AEM) electrolyzer is an emergent technology that combines the advantages of the other two technologies.<sup>31-34</sup>



**Chapter 2 objectives:**

- incorporate amorphous OER catalysts into PEM MEAs

**Chapter 3 objectives:**

- implement plastic flow-field plates into AEM electrolyzers

**Figure 1.1** Cross-section cartoons of the different electrolyzer technologies discussed in this thesis. **(A)** Alkaline electrolyzer cells contain two electrodes immersed in 20-30% KOH that are separated by a separator membrane that are generally made of nickel oxide, asbestos, or polymers. Individual cells are separated by bipolar plates made of nickel or stainless steel in an electrolyzer stack configuration. **(B)** PEM electrolyzers contain flow-field plates that facilitate fluid and gas transport in the devices and are generally made of titanium. These flow-field plates sandwich the MEA that generally comprises of titanium gas diffusion electrodes, platinum group metal catalysts, and a PEM membrane. Individual cells are separated by flow-field plates in the electrolyzer stack configuration. **(C)** AEM electrolyzers contain flow-field plates that facilitate fluid and gas transport in the devices and are generally made of nickel or stainless steel. These flow-field plates sandwich the MEA that generally comprises of nickel or stainless steel gas diffusion electrodes, first-row transition metal oxide catalysts, and an AEM membrane. Individual cells are separated by flow-field plates in the AEM electrolyzer stack configuration.

### 1.3.1 Alkaline Electrolyzers

Alkaline electrolyzers are the most developed electrolyzer technology and are capable of producing hydrogen at the MW scale.<sup>19,30,35-38</sup> The design consists of two electrodes immersed in a liquid electrolyte (e.g., 20-30% KOH) separated by a diaphragm or a separator membrane (Fig. 1.1) such as nickel oxide, asbestos, or polymers that act to separate the product gases (hydrogen and oxygen).<sup>31</sup> The prominent advantage of alkaline electrolyzers is the generally good stability of lower cost metals and electrocatalysts in basic media.<sup>39-47</sup>

There are inherent operational issues with alkaline electrolyzers that include low partial load range (20-40%), efficiency and safety issues at high pressure, and relatively low current densities ( $0.2\text{-}0.4\text{ A cm}^{-2}$ ). Low partial load range and low operating pressure arise because the separator diaphragms employed in alkaline electrolyzers are slightly permeable to gases and fail to prevent cross-diffusion of hydrogen and oxygen at high current densities. Oxygen in high concentrations in the anode chamber can diffuse to the cathode chamber and reduce back to water in the presence of hydrogen, thereby decreasing overall efficiency of electrolysis. Diffusion of hydrogen to the anode chamber will reduce the efficiency of the electrolyzer and will introduce a safety risk if hydrogen levels on the oxygen side of the cell reach 2%.<sup>29</sup> These technological issues limit current densities therefore alkaline electrolyzers tend to be capital intensive.

### 1.3.2 Proton Exchange Membrane Electrolyzers

PEM electrolyzers were first introduced in the 1960s by General Electric and were originally designed to overcome the shortcomings of the alkaline electrolyzer<sup>48</sup> and the spatial constraints

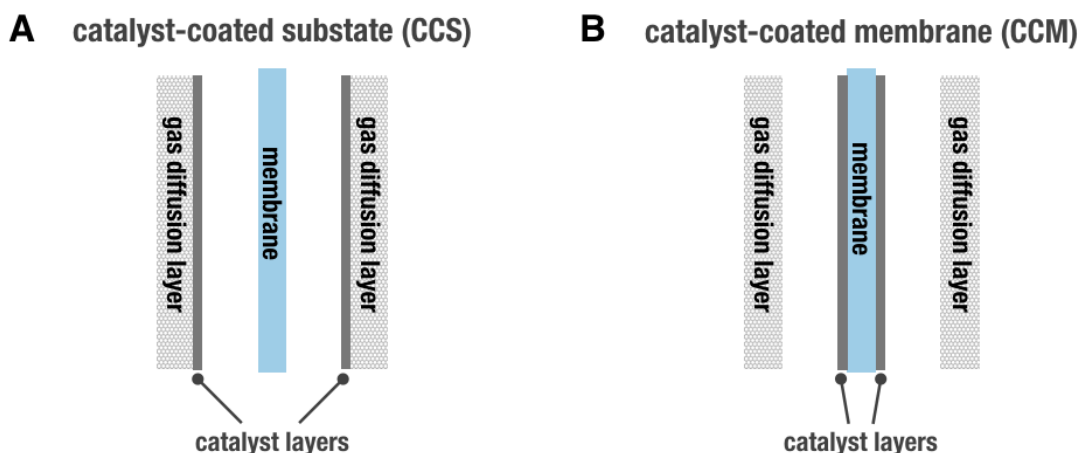
of NASA space missions.<sup>29</sup> The significant design change was the incorporation of a solid polymer electrolyte (SPE) that solved issues of gaseous crossover, improving the overall efficiency of the electrolyzer and enabling high current density operation ( $>1 \text{ A cm}^{-2}$ ).<sup>29</sup>

The MEA and the zero-gap architecture are employed in PEM electrolyzers. Components of the MEA in a PEM electrolyzer include the anode and cathode gas diffusion layers (GDLs), the SPE membrane, and catalyst layers.<sup>49-51</sup> Titanium materials (e.g., titanium felt) are generally used as anode gas diffusion layers. OER catalysts are commonly iridium and ruthenium oxides and HER catalysts are often carbon-supported platinum.<sup>29</sup> The MEA is assembled by sandwiching the membrane between two GDLs with the catalyst layers located at the interfaces between the membrane and GDL (Fig. 1.1). An MEA is housed between two flow-field plates that facilitate the transport of reactants and products to and from the electrochemical reaction sites in the respective catalyst layers (Fig. 1.1). Cells are connected in series making an electrolyzer stack with a higher total active electrochemical surface area of the device. To reduce the amount of material used in an electrolyzer stack, flow-field plates serve as bipolar plates, where one plate acts as the anode or cathode for two separate adjacent cells. These flow-field plates also serve to deliver electricity from a power source to the MEA.<sup>28</sup> Flow-field or bipolar plates must be stable, exhibit high electrical, and thermal conductivity (for waste heat transport away from the MEA) for efficient operation.<sup>29</sup>

The advantage of a PEM electrolyzer relative to an alkaline electrolyzer is that a solid polymer electrolyte membrane, such as Nafion 117, is impermeable to gasses and retains high proton conductivity ( $0.25 \text{ S cm}^{-2}$  at  $80^\circ\text{C}$ ) when fully hydrated.<sup>52</sup> PEM electrolyzers operate at

current densities above  $2 \text{ A cm}^{-2}$  with efficiencies greater than 70%.<sup>39,53</sup> The limited gaseous crossover enables PEM electrolyzers to maintain higher efficiencies at higher current densities without raising the hydrogen concentrations on the oxygen side of the cell.<sup>29</sup> The low permeability of gases through the membrane also facilitates electrolyzer operation at elevated pressures,<sup>28,54,55</sup> reducing energy required to compress hydrogen in the overall electrolysis system.<sup>29</sup> Moreover, the use of a thin ( $\sim 20 - 300 \text{ }\mu\text{m}$ ) ion exchange membrane (e.g., Nafion<sup>®</sup>) reduces the inter-electrode gap in a cell configuration and lowers ionic resistance. PEM electrolyzers are potentially more appropriate for urban installation and other applications with space limitations than alkaline electrolyzers due to the relatively high current densities and efficiencies.

Catalyst layers are generally incorporated into a PEM MEA by two different methods. The catalyst coated substrate (CCS) configuration stipulates that the catalyst was deposited on the GDLs prior to assembly of the MEA (Fig. 1.2A). Conversely, the catalyst-coated membrane (CCM) configuration indicates that the catalyst layer was deposited on the ion exchange membrane before the final assembly of the MEA (Fig. 1.2B).



**Figure 1.2** Schematic of (A) catalyst-coated substrate (CCS) and (B) catalyst-coated membrane (CCM).

CCMs are commonly prepared by a decal method (also known as the transfer method), where the catalyst layer is synthesized or brushed, sprayed, or blade coated on a PTFE sheet decal substrate and then transferred to the membrane via hot-pressing.<sup>56-58</sup> Previous work has shown that PEM electrolyzers that utilize CCMs have a notable improvement in efficiency, citing a more intimate contact between the catalyst layer and the polymer electrolyte.<sup>59</sup> Additional advantages to this configuration include: (i) the catalyst layer effectively adheres to the membrane; (ii) ohmic losses between the catalytic layer and the membrane are reduced due to intimate contact; (iii) CCMs can be easily removed from the stacks for maintenance;<sup>29</sup> and (iv) gas cross-permeation at high operating pressure is reduced because catalyst particles in the subsurface region of the membrane promote the oxidation of permeating hydrogen.<sup>53</sup>

CCSs are generally best employed in a system where the MEA is fully submerged in electrolyte where contact between the catalyst layer and the solid polymer electrolyte is less vital to realize the triple phase boundary. The preparation of CCSs is convenient due to the fact that materials used for GDLs in electrolyzers can survive higher temperatures than solid polymer electrolyte membranes and will not be mechanically damaged by solvents used in deposition techniques (i.e. spray-coating). Electrodeposition<sup>60</sup> may also be used in addition to brush-coated, spray-coated, roll-coated, or blade-coated catalyst layers directly on GDLs followed by thermal deposition.<sup>34</sup>

The electrochemical evolution of oxygen in acidic media is challenging due to the lack of acid-stable OER catalysts.<sup>28,61-66</sup> While various forms of metal oxides have been studied for decades,<sup>61</sup> amorphous phases of metal oxides, including acid-stable iridium oxide, have gained recent attention because of their superior catalysts properties.<sup>65,67-77</sup> The synthesis of robust amorphous iridium films in a scalable manner can be challenging. The majority of reported amorphous metal oxides were synthesized by electrodeposition<sup>67,69,73-75</sup> and physical vapor deposition.<sup>40,78,79</sup> The use of electrodeposition of amorphous iridium oxide is limited to deposition on electrically conductive substrates (i.e. conductive glass) and physical vapour deposition requires expensive equipment like vacuum chambers, high intensity ion or electron beam emitters, and bulk metal targets. The Berlinguette group has demonstrated photodeposition by ultraviolet-driven decomposition (UVDD) of photoactive, metal-organic precursors as a viable means of accessing amorphous metal oxide films, providing an alternative means of



accessing these acid-stable catalytic films. This deposition method is non-aqueous and occurs at low temperature ( $<50\text{ }^{\circ}\text{C}$ ) and at atmospheric pressure.

Chapter 2 highlights the incorporation of amorphous iridium oxides thin films into membrane electrode assemblies (MEAs) by developing an amorphous catalyst-coated membrane (CCM). Nafion 117 served as the archetype solid polymer electrolyte membrane for this study and amorphous iridium oxide was chosen as the electrocatalyst because of its stability in highly acidic environments. UVDD was shown to decompose amorphous thin films on Teflon substrates, enabling the use of decal transfer of amorphous metal oxides to produce amorphous CCMs. The intent of depositing amorphous thin films on the polymer electrolyte membrane was to reduce electrocatalyst loading and retain intimate contact between the electrocatalyst layer and the polymer electrolyte, increasing the overall catalyst utilization. This method enables any photodeposited thin-film metal oxide composition to be deposited on any ion conducting polymer membrane.

### **1.3.3 Anion Exchange Membrane Electrolyzers**

PEM electrolyzers operate in acidic media ( $\text{pH} < 1$ ) and thus require platinum group metals (PGMs) such as iridium for the electrocatalyst layers.<sup>29,40,80</sup> The acidic environment also necessitates flow-plate and GDL components made from titanium for chemical stability.<sup>29,81,82</sup> The AEM architecture consolidates the advantages the PEM and alkaline electrolyzers.<sup>31-34</sup> The ionic conductivities of state-of-the-art AEMs with  $\text{OH}^-$  form are similar to commercial PEMs, but they are currently more sensitive to hydration and temperature, and are susceptible to  $\text{CO}_2$  contamination.<sup>31</sup>

There are currently very few reports of AEM electrolyzers in the literature. Leng *et. al.* reported an AEM electrolyzer that achieved a current density of  $1 \text{ A cm}^{-2}$  with a voltage efficiency of 74% using iridium dioxide at the anode and a platinum cathode.<sup>33</sup> A related AEM electrolyzer that instead used nickel-iron oxide coated nickel anodes (and platinum cathodes) also achieved a current density of  $1 \text{ A cm}^{-2}$  with similar efficiency.<sup>41</sup> Pavel *et. al.* demonstrated that a  $\text{CO}_2$  tolerant electrolyte helped maintain a steady current for 1000 h at  $470 \text{ mA cm}^{-2}$  (efficiency = 72%).<sup>32</sup> Xiao *et. al.* demonstrated an AEM electrolyzer using pure water instead of potassium hydroxide produced  $0.4 \text{ A cm}^{-2}$  at a voltage efficiency of >80%.<sup>34</sup> AEM research to date is generally conducted in repurposed PEM cells, sometimes using materials such as titanium that are not ideal for use in basic environments.<sup>31-34</sup> The construction costs associated with developing AEM test cells may impede the research of AEM devices.

In Chapter 3, I report a strategy for lowering capital costs of the unit by using 3D-printed plastic as a stand-in material for the metal used in field-flow plates that channel water and gas flow through the electrolyzer cell. This goal was achieved by successfully electroplating nickel onto 3D-printed plastic, a process that has not been previously achieved. The test cells containing these metal-coated plastic components matched the performance of conventional metal electrodes, while reducing the metal content that would otherwise be used in the cell. Moreover, the ability to electroplate 3D-printed parts offers the opportunity to rapidly prototype flow-field geometries for electrolysis applications.

## Chapter 2: Integrating Amorphous Iridium Oxide into Membrane Electrode Assemblies

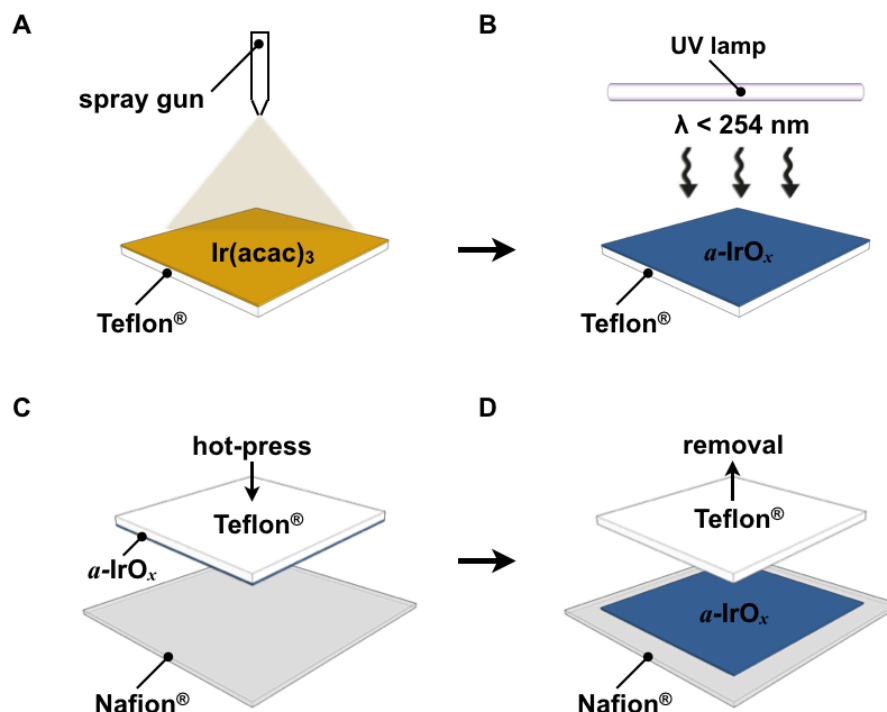
### 2.1 Introduction

Conventional electrolyzers operate with a strongly alkaline electrolyte and an environment where many transition metal OER catalysts are stable. Proton exchange membrane (PEM) electrolyzers, on the other hand, utilize solid polymer electrolytes (e.g. Nafion) that operate in acidic media where only expensive metal oxides, such as iridium, are capable of mediating the OER.<sup>29</sup> IrO<sub>x</sub> is currently the best option for PEM electrolyzers because of its high stability in acid and high OER activity.<sup>61,62,83-85</sup> PEM electrolyzers exhibit higher current densities, efficiencies, and lower gas crossover at high current densities than alkaline electrolyzers,<sup>39</sup> but iridium is exceedingly expensive.<sup>86</sup> PEM electrolyzers therefore require a significant reduction in iridium loadings from a few mg cm<sup>-2</sup> to *ca.* 0.1 mg cm<sup>-2</sup> in order to be economically attractive.<sup>87</sup>

The study of OER catalysts in basic media has shown that amorphous materials are more efficient electrocatalysts than crystalline phases.<sup>65,67-75,77</sup> Amorphous phases of iridium oxide (*a*-IrO<sub>x</sub>) can also provide an energy savings compared to crystalline IrO<sub>2</sub>.<sup>76</sup> The use of *a*-IrO<sub>x</sub> therefore offers a means of using less iridium in PEM electrolyzers. This opportunity first requires a method to incorporate these amorphous catalyst layers into MEAs suited for PEM electrolyzers, an issue that is addressed in this chapter.

The deposition of a catalyst layer directly on the surface of a membrane to form a CCM for use in a PEM MEA has been previously documented.<sup>59</sup> This CCM configuration displays a higher efficiency than a MEA with a CCS, where the electrocatalyst is deposited directly on the GDL. This difference in performance is likely due to the CCM configuration having a better catalyst-membrane interface that better utilizes the catalyst layer.<sup>88,89</sup> A challenge in using CCMs is that the Nafion membrane swells when catalysts are applied when exposed to solvents.<sup>57</sup> Moreover, the formation of  $\alpha$ -IrO<sub>x</sub> films by electrodeposition<sup>73-75</sup> and photodeposition<sup>76</sup> techniques directly on Nafion cannot be done. Electrodeposition requires electrically conductive surfaces and UV-driven decomposition (UVDD) promotes fluorinated radical formation that will cause Nafion to degrade.<sup>90,91</sup>

The decal transfer method offers a means to overcome the issue of exposing Nafion to solvents.<sup>57</sup> The membrane is never exposed to solvents because the catalyst is first deposited on a sacrificial substrate (e.g., Teflon) that is then used to transfer the catalysts onto the membrane using pressure and heat.<sup>56</sup> Deposition on a non-conductive Teflon substrate can be accomplished using UVDD because this method utilizes light instead of a conductive electrode to form  $\alpha$ -IrO<sub>x</sub> catalyst layers. It is shown herein that the UVDD preparation of  $\alpha$ -IrO<sub>x</sub> on Teflon enables the use of decal transfer to prepare CCMs with  $\alpha$ -IrO<sub>x</sub> that can be used in PEM electrolyzers (Fig. 2.1).



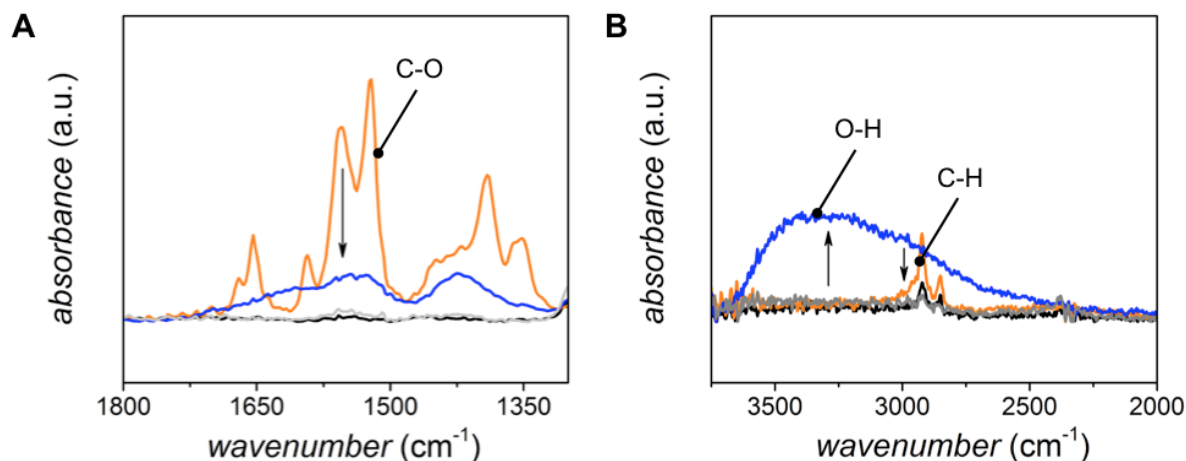
**Figure 2.1** (A) Precursor  $[\text{Ir}(\text{acac})_3]$  spray-coated onto a Teflon substrate. (B) UVDD of sprayed-coated  $\text{Ir}(\text{acac})_3$  on a Teflon sheet to produce a thin film of  $a\text{-IrO}_x$ . (C) Decal transfer using a hot press at variable temperatures and pressures. (D) Teflon decal substrate peeled from Nafion to reveal the final CCM. See Appendix for photos.

## 2.2 Results

### 2.2.1 Decal Transfer Method

A multi-step process was used to yield an  $a\text{-IrO}_x/\text{Nafion}$  CCM following the procedure described in Figure 2.1. Iridium acetylacetonate ( $\text{Ir}(\text{acac})_3$ ) was dissolved in chloroform and spray-coated onto a 0.23-mm thick Teflon substrate. The film was then photolyzed with UV radiation ( $\lambda_{\text{max}} \sim 185$  and  $254 \text{ nm}$ ;  $\sim 10 \text{ mW cm}^{-2}$ ) for 7 h to drive off the ligand and form  $a\text{-IrO}_x$  quantitatively. The progress of this decomposition process was tracked by Fourier transform

infrared spectroscopy (FTIR), which probes the vibrational modes of the ligands (Fig. 2.2). We observed the disappearance of the absorption bands corresponding to the vibrational modes of the C-O bonds (ca.  $1500\text{ cm}^{-1}$ )<sup>92</sup> and C-H bonds (ca.  $3000\text{ cm}^{-1}$ )<sup>92</sup> of the acetylacetonate ligands over 7 h of UV photolysis. The growth of the broad absorbance band centered near  $3200\text{ cm}^{-1}$  was observed and attributed to chemisorbed oxyhydroxide on the surface of the  $\alpha\text{-IrO}_x$  film.<sup>92</sup> The decal transfer step was achieved by sandwiching the catalyst coated side of the Teflon substrate with the dry Nafion membrane and applying different pressures and temperatures using a hot-press for one minute. The Teflon substrate was then peeled from the Nafion membrane leaving the  $\alpha\text{-IrO}_x$  catalyst layer imbedded on the membrane. FTIR experiments after the transfer of the blue-grey catalyst film showed the loss of the broad oxyhydroxide absorbance band centered near  $3200\text{ cm}^{-1}$  indicating the successful transfer of  $\alpha\text{-IrO}_x$ . This process yielded CCMs with catalyst loadings of  $0.03\text{ mg cm}^{-2}$  ( $\sigma = 0.01\text{ mg cm}^{-2}$ ).



**Figure 2.2** FTIR spectra recorded on blank Teflon decal transfer substrate (*black*), Ir(acac)<sub>3</sub>-coated Teflon substrate (*orange*), *a*-IrO<sub>x</sub>/Teflon film on Teflon substrate after 7 h of UV radiation (*blue*), and Teflon substrate after decal transfer (*grey*). Absorption bands are associated with the vibrational modes of (A) C-O bonds (*ca.* 1500 cm<sup>-1</sup>) and (B) C-H bonds (*ca.* 2800 cm<sup>-1</sup>) of the acetylacetonate ligand and vibrational modes of O-H bonds (broad peak centered *ca.* 3300 cm<sup>-1</sup>) of chemisorbed oxyhydroxide.

The decal transfer process was optimized by examining the transfer of *a*-IrO<sub>x</sub> from the Teflon substrate at different temperatures and pressures (Table 2.1). The glass transition temperature ( $T_{glass}$ ) of Nafion<sup>®</sup> 117 (115 °C),<sup>93</sup> and thus temperatures slightly below (100 °C) and above (125 °C) were tested as well as the higher temperature of 200 °C (Nafion<sup>®</sup> 117 degrades at > 250 °C).<sup>93</sup> Three different pressures were also surveyed: 100 psi; 500 psi; and 1000 psi. All decal transfers were performed for 1 min. Complete decal transfer was observed at 125 °C for pressures of 500 and 1000 psi. Decal transfer at 100 °C did not transfer the catalyst uniformly to the Nafion, while at 200 °C the Nafion adhered to the aluminum foil used as a heat-conducting, protective layer during hot pressing. The CCMs produced at 125 °C and 1000 psi were therefore

used for electrochemical investigations. Note that all CCMs were annealed at 150 °C for one hour prior to electrochemical experiments to promote catalyst adhesion to the membrane.

**Table 2.1** Temperatures and pressures tested in decal transfer study of  $\alpha$ -IrO<sub>x</sub>/Nafion.

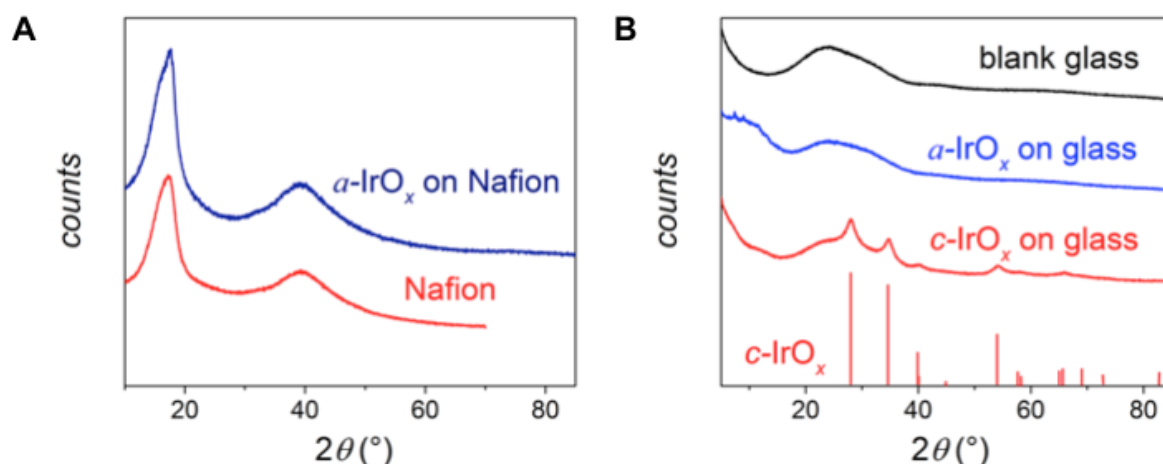
temperature (°C)	pressure (psi)	observation
100	100	partial transfer
100	500	partial transfer
100	1000	partial transfer
125	100	partial transfer
<b>125</b>	<b>500</b>	<b>successful transfer</b>
<b>125</b>	<b>1000</b>	<b>successful transfer</b>
200	100	Nafion adhesion to aluminum
200	500	Nafion adhesion to aluminum
200	1000	Nafion adhesion to aluminum

## 2.2.2 Physical Characterization of Amorphous Catalyst-Coated Membranes

Cognizant that the exposure of  $\alpha$ -IrO<sub>x</sub> to high temperature and pressure can crystallize amorphous films,<sup>65,76</sup> powder X-ray diffraction (pXRD) experiments were conducted to confirm that the film was still amorphous after decal transfer at 125 °C and 1000 psi and subsequent annealing at 150 °C. The XRD data on the CCMs revealed no crystalline peaks to suggest that the catalyst layer underwent a phase change (Fig. 2.3A). Given the possibility that the  $\alpha$ -IrO<sub>x</sub> film on the Nafion was not thick enough to produce Bragg reflections, I tested a deposited and photolyzed  $\alpha$ -IrO<sub>x</sub> on a glass slide that was then hot-pressed at 1000 psi and 125 °C. No



crystalline peaks were observed under these decal transfer conditions (Fig. 2.3B). To confirm there was an adequate amount of catalyst material on the glass, the same film was annealed at 500 °C for one hour to induce crystallization. The heated films produced reflections that matched that of crystalline IrO<sub>2</sub> (JCPDS 15-790), with strong diffraction peaks at  $2\theta = 28.0^\circ$ ,  $34.6^\circ$ ,  $40.0^\circ$ , and  $53.4^\circ$ .

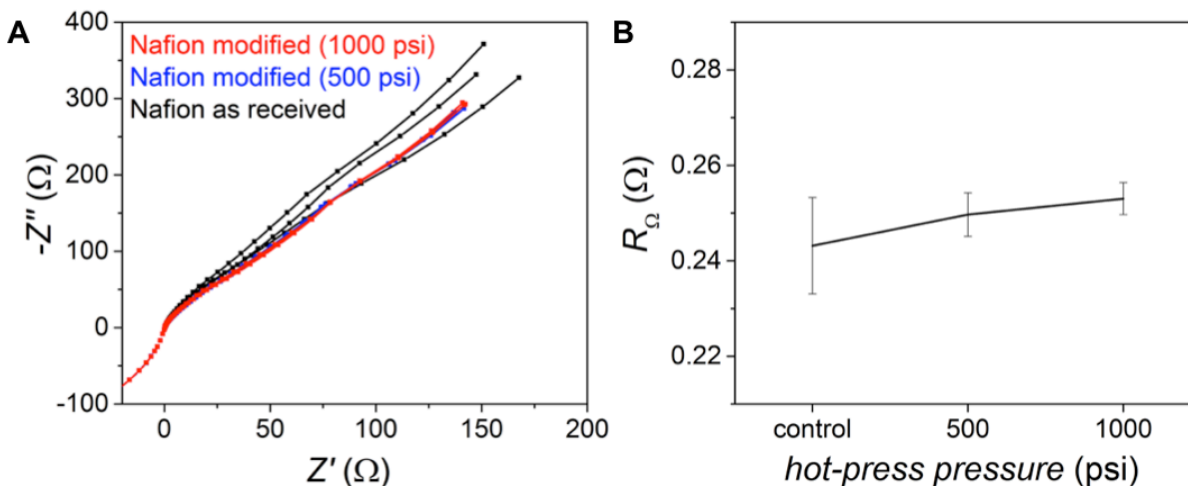


**Figure 2.3** Powder XRD data acquired on (A) *a*-IrO<sub>x</sub> CCM prepared by decal transfer at 125°C and 1000 psi (*blue*), and a blank Nafion membrane (*red*); and (B) *a*-IrO<sub>x</sub> coated glass (*blue*) that underwent hot-pressing conditions of 125°C and 1000 psi for 1 min, the same sample after being heated at 500°C for 1 h (*red*), and blank glass (*black*). Powder XRD pattern (*red lines*) for crystalline IrO<sub>2</sub> (JCPDS 15-790) are shown for reference.

### 2.2.3 Effect of CCM Modification on the Ionic Conductivity of Nafion

Ionic resistance contributes to the overall ohmic resistance of an electrolyzer cell,<sup>94</sup> and thus the ionic conductivity of Nafion must not be compromised during the formation of the CCM. The main contribution to the measured impedance of the in-plane measurement comes

from the bulk membrane, while the contributions from the interfacial resistances between the membrane and the electrodes are dominate in the through-plane measurements.<sup>95</sup> The effects of CCM modification on the ionic conductivity of the membrane were therefore tested with through-plane measurements of the membrane sandwiched between two titanium flat plate electrodes. The electrical resistance through the titanium plates, the contact resistance between the plates and the membrane, and the contact resistance through any electrical connections (i.e. alligator clips) were assumed to be constant during all alternating current electrochemical impedance spectroscopy (EIS) experiments. Three cleaned Nafion membranes were used for all EIS measurements. Two membranes were hot-pressed at 500 psi and 1000 psi and annealed at 150 °C prior to testing. All EIS measurements were done in a 2-electrode setup with 3 cm<sup>2</sup> of membrane surface in contact with both plates, while submerged in 0.5 M H<sub>2</sub>SO<sub>4</sub> electrolyte. The surfaces of the titanium plates that were not in contact with the membrane were masked with Kapton tape. The resultant data was plotted in a Nyquist plot (Fig. 2.4A) and the total ohmic cell resistance ( $R_{\Omega}$ ) was taken to equal the value of the real impedance at  $-Z''$  equals zero.<sup>96</sup> The resulting cell resistances (Fig. 2.4B) show that hot-pressing at 500 or 1000 psi and annealing at 150 °C has a negligible effect on the ionic resistance observed during through-plane measurement on the modified membranes and therefore the modification of the membrane during the decal transfer procedure has no effect on the ionic conductivity of the amorphous CCM.

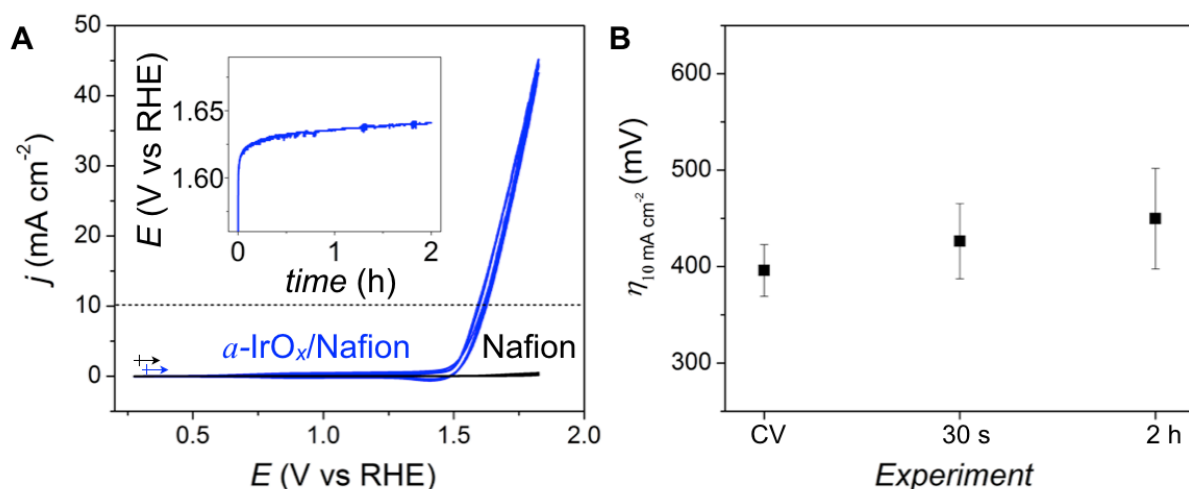


**Figure 2.4** (A) Nyquist plots of through-the-plane impedance responses of Nafion membranes as received (*black*), hot-pressed at 500 psi and 125 °C and annealed at 150 °C (*blue*), and hot-pressed at 1000 psi and 125 °C and annealed at 150 °C (*red*). (B) Ohmic resistances of hot-pressed membranes determined by through-plane measurements.

#### 2.2.4 Electrochemical Characterization of Amorphous Catalyst-Coated Membranes

The electrochemical response of the  $\alpha$ -IrO<sub>x</sub>/Nafion CCMs was investigated in a custom 3-electrode cell and a 0.5 H<sub>2</sub>SO<sub>4</sub> electrolyte using cyclic voltammetry and chronopotentiometry techniques. The CCM was interfaced with Toray carbon paper (porosity = 78%; thickness = 190 μm) on the anode side for initial electrochemical testing (it is recommended that in future studies this gas diffusion layer material be replaced with titanium felt or foam because oxidation of the carbon electrodes can occur). The CCM was sandwiched between the Toray carbon paper and a platinum mesh counter electrode to make up an MEA used for testing. Sustained electrocatalysis at a current density of ~40 mA cm<sup>-2</sup> at 1.75 V vs RHE was measured (Fig. 2.5A). An uncoated Nafion membrane was used in the same MEA configuration as a control and showed a current density of <1 mA cm<sup>-2</sup> at 1.8 V vs RHE (Fig. 2.5A). These results were reproduced on multiple

CCM samples produced at different times using the same method. A reduction in performance of  $\sim 30$  mV was observed over 2 h of operation at a current density of  $10 \text{ mA cm}^{-2}$  (Fig. 2.5B). The catalytic performance of the  $\alpha\text{-IrO}_x/\text{Nafion}$  is within the range of sputtered and electrodeposited amorphous  $\text{IrO}_x$  previously reported in literature at  $10 \text{ mA cm}^{-2}$  (Table 2.2), our cell fails to reach current densities that are comparable to contemporary PEM electrolyzers ( $>1 \text{ A cm}^{-2}$ ).



**Figure 2.5** Electrochemical behavior of CCMs that underwent decal transfer at  $125^\circ\text{C}$  and 1000 psi for 1 min. (A) Cyclic voltammograms recorded ( $\nu = 10 \text{ mV s}^{-1}$ ) on  $\alpha\text{-IrO}_x$  film deposited on Nafion (blue) and blank Nafion (black). Inset: Chronopotentiometry recorded on  $\alpha\text{-IrO}_x$  film deposited on Nafion at a anodic current density of  $10 \text{ mA cm}^{-2}$ . (B) Reproducibility of overpotential needed to achieve  $10 \text{ mA cm}^{-2}$  recorded on  $\alpha\text{-IrO}_x$  films deposited on Nafion recorded during the cyclic voltammogram (CV) and chronopotentiometry experiments at 30 s and 2 h. Electrochemistry conditions: counter electrode = Pt mesh; reference electrode =  $\text{Ag/AgCl}$ ,  $\text{KCl}$  (sat'd); cyclic voltammogram scan rate =  $10 \text{ mV s}^{-1}$ ; chronopotentiometry current density =  $10 \text{ mA/cm}^2$ ; electrolyte =  $0.5 \text{ M H}_2\text{SO}_{4(aq)}$ .

**Table 2.2** OER activities of  $\alpha$ -IrO<sub>x</sub> films.

preparation method	overpotential at 10 mA/cm <sup>2</sup> (mV)	reference
electrodeposition	430 <sup>a</sup>	74
sputtering	300 <sup>a</sup>	40
UVDD + decal transfer	396	this work

<sup>a</sup>experiments conducted on thin film electrocatalysts deposited on conductive glass substrates

### 2.3 Summary

It is reported here a decal transfer method for incorporating  $\alpha$ -IrO<sub>x</sub> into a Nafion membrane. I used UVDD to deposit thin films of  $\alpha$ -IrO<sub>x</sub> on a hydrophobic, nonconductive Teflon. A survey of decal transfer parameters revealed optimal hot-pressing conditions to be 125 °C and 1000 psi. The CCMs produced at these conditions resulted in a catalyst loading of 0.03 mg cm<sup>-2</sup> ( $\sigma$  = 0.01 mg cm<sup>-2</sup>) and demonstrated an activity toward the OER of 10 mA/cm<sup>2</sup> at an overpotential of 396 mV ( $\sigma$  = 26.9 mV) during cyclic voltammetry experiments. The CCMs show reasonable stability, exhibiting a reduction in performance of ~30 mV during steady state current density of 10 mA/cm<sup>2</sup> for 2 h. Our results closely compare to past  $\alpha$ -IrO<sub>x</sub> benchmarks deposited on conductive glass from the literature. Hence, the decal transfer method provides a facile way to produce low-loading CCMs with amorphous electrocatalysts possessing high activity towards the OER. Furthermore, this approach is envisaged to have the versatility to be applied to the transfer of amorphous thin films to substrates for applications additional to electrolyzers that may be damaged during conventional deposition techniques.

## **2.4 Methods**

### **2.4.1 Materials**

Iridium (III) acetylacetonate (Strem, 98%), chloroform (Fisher Scientific, reagent grade), and sulfuric acid (Sigma Aldrich, reagent grade) were used as received and without further purification. Titanium felt (porosity = 56%; thickness = 200  $\mu\text{m}$ ) was purchased from Bekaert. Nafion N117 (thickness = 177  $\mu\text{m}$ ) and Toray carbon paper (porosity = 78%; thickness = 190  $\mu\text{m}$ ) were purchased from Fuel Cell Ect.. Teflon was sourced from Chemistry Department Mechanical Engineering with special thanks to Des Lovrity.

### **2.4.2 Sample Preparation**

Nafion N117 membranes were cut into squares ( $2.8\text{ cm} \times 2.8\text{ cm}$ ) with geometric surface areas of  $7.8\text{ cm}^2$ . The membranes were submerged in 50 mL of 3 wt.%  $\text{H}_2\text{O}_2$  and stirred at 800 rpm for 10 min then submerged in a 100 mL bath of boiling 0.5 M  $\text{H}_2\text{SO}_4$  and stirred at 800 rpm for 60 min. Excess acid and  $\text{H}_2\text{O}_2$  on the surface of the membranes were removed with compressed nitrogen before the next cleaning step. The membranes were then dehydrated in a vacuum oven at room temperature and a pressure of 0.8 atm for at least 12 h. The dehydrated membranes were used for decal transfer procedure.

Teflon decal transfer substrates were cut into squares ( $2.2\text{ cm} \times 2.2\text{ cm}$ ) with geometric surface areas of  $4.8\text{ cm}^2$ . Teflon decal transfer substrates were cleaned by sonication in acetone for 5 min prior to use. Titanium felt and Toray carbon paper were cut into ( $2.5\text{ cm} \times 2.5\text{ cm}$ ) with geometric surface areas of  $6.3\text{ cm}^2$ . These gas diffusion layers were cleaned by sonication in

acetone for 5 min, dried, sonicated in 1.0 M  $\text{H}_2\text{SO}_4$  for 5 min. The gas diffusion layers were then washed with deionized water and then sonicated in deionized water for 5 min.

$\text{IrO}_x/\text{Teflon}$  was synthesized by spray coating a 0.01 M  $\text{Ir}(\text{acac})_3$  solution (83.4 mg of  $\text{Ir}(\text{acac})_3$  in 25.38 g of chloroform) on the surface of a thin Teflon decal transfer substrate (0.127 mm), using a gravity fed B-200 Beaver airbrush. Spray coating applied  $\sim 0.1 \text{ ml/cm}^2$  of 0.01 M  $\text{Ir}(\text{acac})_3$  solution on the Teflon surface. The film was irradiated by UV light for at least 12 h to insure photodecomposition of the catalyst precursors. The spray coat procedure was repeated for each additional deposition layer. Catalyst loading was determined gravimetrically.

Decal transfer was done using a Dake Hot-press model 44226. The cathode side of the membrane was not heated and a 2 cm thick, protective block of Teflon was placed between the hot press plate and Nafion membrane. The anode side was heated to the stated temperature and aluminum foil was placed between the  $\alpha\text{-IrO}_x/\text{Teflon}$  and the hot pressed plate. To perform the decal transfer, the Nafion membrane was sandwiched between the cathode-side protective Teflon and the  $\alpha\text{-IrO}_x/\text{Teflon}$ .

The membrane electrode assembly was prepared by mechanically pressing a platinum mesh counter electrode (Aldrich) on the cathode side, the prepared Nafion membrane (Ion Power), and a titanium felt (Bekaert) or Toray paper on the anode side between two Ti plate electrodes (McMaster-Carr).

### 2.4.3 Physical Methods

Electrochemical measurements were performed in 0.5 M  $\text{H}_2\text{SO}_4$  electrolyte with a CH Instruments 660D potentiostat. CCMs were hydrated in 0.5 M  $\text{H}_2\text{SO}_4$  for at least 12 h before

electrochemical experiments. Measurements were performed in a customized three-electrode test cell using a Ag/AgCl (sat. KCl) reference electrode calibrated against a reversible hydrogen electrode (RHE) in 0.5 M H<sub>2</sub>SO<sub>4</sub> electrolyte. Cyclic voltammograms were acquired at a 10 mV s<sup>-1</sup> scan rate. No aggregation was induced on the test cell besides that from evolved gaseous products.

FTIR spectroscopy was recorded on a Bruker Alpha spectrometer using an ATR platinum diamond accessory. Absorbance data were collected from 4000 cm<sup>-1</sup> to 400 cm<sup>-1</sup> using 48 scans and 4 cm<sup>-1</sup> resolution. XRD data were recorded with a Bruker D8 Advance diffractometer using Cu K $\alpha$  radiation. Data were collected between 2 $\theta$  angles of 5° and 90° with a step size of 0.04°. The step time was 1.6 s.



## Chapter 3: Electroplating Enables 3D-Printed Components Tailored for Water Electrolysis

### 3.1 Introduction

The electrolysis of water into hydrogen and oxygen fuels represents a potentially scalable solution for storing renewable electricity.<sup>1,15,97,98</sup> The most widely used commercial electrolyzers are alkaline electrolyzers capable of maintaining high current densities ( $>200 \text{ mA cm}^{-2}$ ) for several years, but few of these units are currently used for energy storage applications.<sup>6</sup> There has therefore been significant efforts directed at developing new electrolyzer technologies and architectures that are capable of producing hydrogen more cost effectively.<sup>28,99,100</sup> Proton-exchange membrane (PEM) electrolyzers are an emergent technology capable of reaching substantially higher current densities ( $>1 \text{ A cm}^{-2}$ ), but the costs associated with the membrane and acid-stable catalyst remain a challenge.<sup>29</sup> The incorporation of a membrane in alkaline electrolyzers has also been shown to be a promising approach to driving up current densities,<sup>32,33,101</sup> but the long-term stability of the membranes remains a fundamental issue to deployment.<sup>31</sup>

These advances in electrolyzer cell engineering, in tandem with the global scientific pursuit for new electrocatalysts,<sup>40,65,69-71,102-105</sup> have driven improvements in electrolyzer efficiencies that make electrolytic hydrogen generation increasingly compelling. Notwithstanding, the capital costs associated with electrolyzers remains strikingly high: 850-5000\$USD/kW.<sup>106</sup>

These high costs will inherently suppress technology adoption, particularly for smaller units where capital costs figure more prominently in the total cost of ownership, and provides the impetus to evaluate ways to lower the cost of the units.<sup>30</sup>


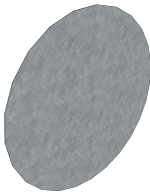
An electrolyzer stack consists of a MEA, balance-of-stack, flow-field and separator plates, which all account for approximately half the overall capital costs.<sup>30,39</sup> Considering that the flow-field and separator plates account for approximately half of the electrolyzer stack cost, nickel and stainless steel accounts for one-quarter of an alkaline electrolyzer unit. The mass of these plates also contribute to significant shipping and handling costs. This observation prompted us to explore whether plastic could be used as a surrogate flow-plate material to lower the materials and manufacturing costs of the electrolyzer unit. Indeed, a first-principles techno-economic analysis for both conventional and contemporary “zero-gap” electrolyzers indicates that the raw materials costs of the bipolar plate could be reduced by half if the nickel were replaced by nickel-coated polylactic acid (**Ni:PLA**) (Table 3.1). These costs savings are even more substantial in cases where **Ni:PLA** replaces stainless steel components, as well as titanium that may be found in other electrolyzer architectures. More strikingly, replacing the metal plates with metal-coated plastics could reduce the weight of each component by *ca.* 7-fold, which will inherently lower the shipping and manufacturing costs associated with the construction of each unit.

While the notion of using plastic is appealing, the implementation of such a material is challenged by fundamentally low conductivities. This issue has previously been addressed by coating plastic with a conductive metal layer such as gold and silver.<sup>107</sup> An alternative strategy

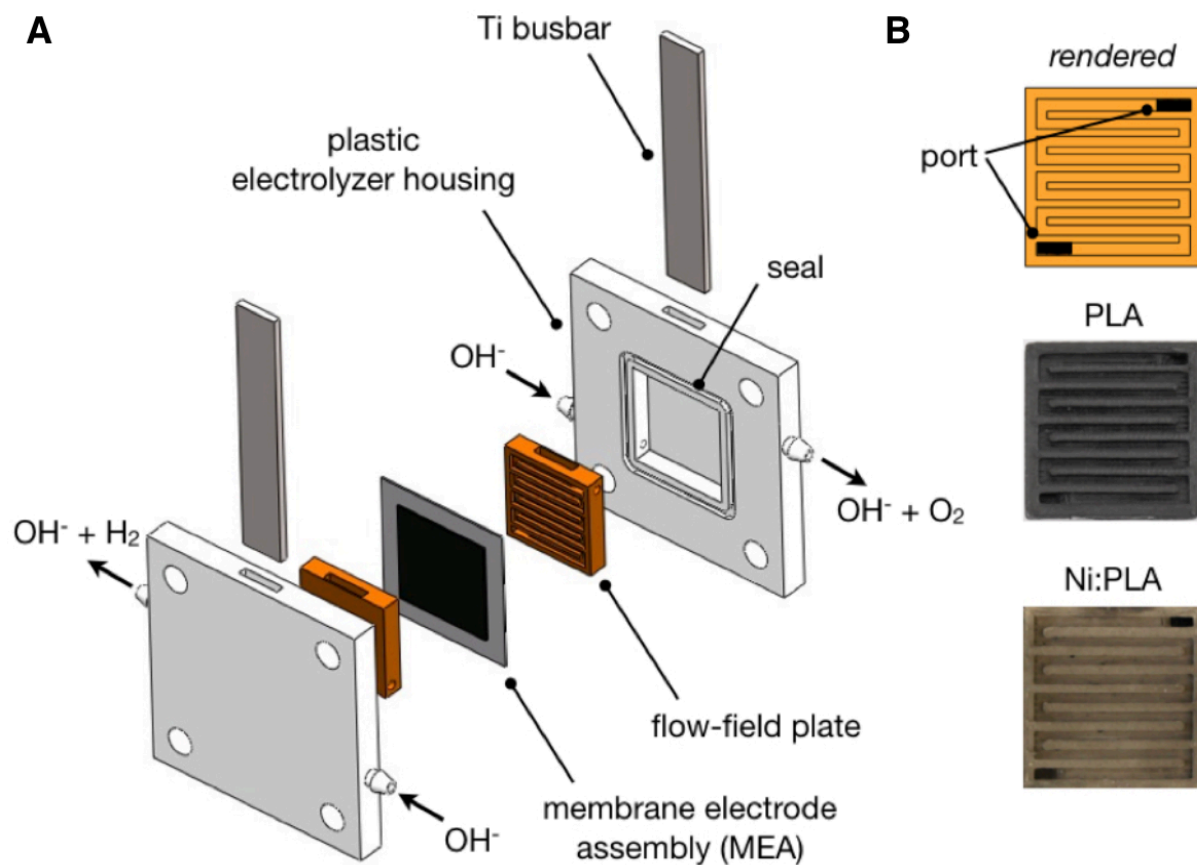
is to incorporate plastic with cheaper conductive and catalysts coatings that do not suffer from corrosion and delamination during electrolysis. This goal has not yet been documented due to the challenges associated with depositing pure metal oxide films relevant to OER catalysis onto non-conducting substrates.

In this chapter we report an electrodeposited metal film on 3D-printed plastic, and we have translated this achievement to the construction of a flow-field plate for OER electrolysis. While the electroplating of plastic has been demonstrated on carbon-doped high density polyethylene,<sup>108</sup> doing the same on 3D-printed conductive plastic has not been previously done due to the prohibitively high resistivities common to composite polylactic acid (PLA) or acrylonitrile butadiene styrene (ABS) thermoplastics. We therefore canvassed a series of conductive thermoplastics and found a PLA filament with sufficiently low resistivities ( $<20\ \Omega\text{ cm}$ ) to accommodate the electroplating of catalytic nickel hydroxide on 3D-printed flow-field plates (Fig. 3.1). This proof-of-concept study confirmed that the electroplated plastic flow-field plates yield electrocatalytic performance parameters are comparable to solid nickel flow-field plates, supporting the notion that plastic may be implemented into electrolyzers to a greater extent than currently used. Moreover, the ability to 3D-print flow-field plates would be a tremendous asset for rapid prototyping that are challenging to do with solid metal substrates.<sup>109</sup>

**Table 3.1** Normalized mass and raw materials cost of two common electrolyzer bipolar plates

	zero-gap <sup>α</sup>		planar <sup>β</sup>	
				
	mass	cost	mass	cost
<b>Ni:PLA<sup>c</sup></b>	1	1	1	1
Nickel	5.5	1.8	6.8	1.9
Stainless Steel	4.8	2.3	6.0	2.5
Titanium	2.8	2.8	3.5	3.0

<sup>α</sup>Zero-gap flow field plate containing channels to enable fluid flow along the separator. Cross sectional and thickness assumed to be 25 cm<sup>2</sup> and 3 cm, respectfully. <sup>β</sup>Planar flow-field plate used in large-scale alkaline electrolyzers. Cross sectional area and thickness assumed to be 2500 cm<sup>2</sup> and 3 cm, respectfully. More details provided as Supporting Information. <sup>c</sup>3D-printed polylactic acid with electroplated nickel coating (*thickness* = 25 μm).



**Figure 3.1** Electrolyzer test cell. (A) Schematic of an exploded flow-plate test cell used in this study. Each 3D-printed electrolyzer housing is made of non-conductive ABS plastic and accommodates the titanium busbars and 3D-printed flow-field plates that are separated by the MEA. The MEA consists of Ni foam gas diffusion layers hot pressed onto each side of a Zirfon™ Perl UTP hydroxide conducting membrane. (B) Drawings (top) and photographs of 3D-printed PLA flow-field plate before (middle) and after electroplating (bottom) with nickel. The single serpentine flow-field pattern was used for all electrochemical studies in this study.

## 3.2 Results

### 3.2.1 Electroplating 3D-Printed Plastic

3D-printed rectangular blocks ( $20\text{ mm} \times 10\text{ mm} \times 2\text{ mm}$ ) were constructed from three commercially available conductive composite plastics based on ABS and PLA to evaluate the volumetric resistivities of each plastic. The resistance perpendicular to the printing plane was at least five-fold higher than that measured parallel to the printing plane in the case of the ABS substrates, but only two-fold higher for the PLA (Table 3.2). The resistivities of the ABS substrates were substantial ( $>500\ \Omega\text{ cm}$ ), while the PLA filament yielded a resistivity of  $<20\ \Omega\text{ cm}$ . These differences in resistivities played a critical role in the electroplating of nickel from a Watt's nickel electroplating solution<sup>110</sup>: Islands were deposited on planar ABS substrates, while uniform films were deposited on planar PLA substrates (Fig. 3.2). This outcome provided the first documented case of electrodeposition on a 3D-printed plastic, and leaves open the possibility that PLA can be used as a structural material for conducting plates where current flow would occur through the conductive shell.

**Table 3.2** Volumetric resistivity of conductive 3D-printing filaments.

plastic filament <sup>1</sup>	resistivity <sup>2</sup> ( $\Omega$ cm)		electroplated film thickness
	parallel	orthogonal	
ABS A <sup>3</sup>	6000	30000	— <sup>6</sup>
ABS B <sup>4</sup>	500	3000	— <sup>6</sup>
PLA <sup>5</sup>	20	40	13 $\mu$ m

<sup>1</sup>ABS = acrylonitrile butadiene styrene; PLA = polylactic acid. <sup>2</sup>With respect to printing plane.

<sup>3</sup>Reprapper Conductive ABS. <sup>4</sup>MatterHackers Conductive ABS <sup>5</sup>Proto-Pasta Conductive PLA.

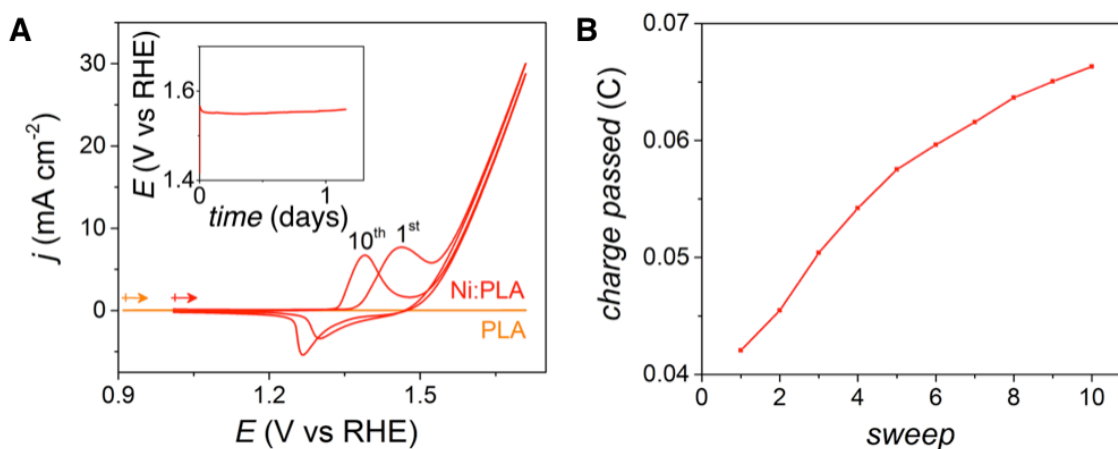
<sup>6</sup>Electroplating could not be achieved.



**Figure 3.2** Electroplating comparison on 3D-printed electrodes. **Left:** Reprapper Conductive ABS, **Middle:** MatterHackers Conductive ABS, **Right:** Proto-Pasta conductive PLA.

We tested the electrocatalytic properties of the planar PLA substrates containing the electroplated nickel by cyclic voltammetry at pH 14 over the 1.0 - 1.8 V range (Fig. 3.3A). The first 10 scans of the cyclic voltammograms (CVs) recorded at a scan rate of 10 mV s<sup>-1</sup> revealed a response consistent with electrocatalysis and reached a current density of ~30 mA cm<sup>-2</sup> at 1.8 V vs RHE. Chronoamperometry experiments were conducted to determine the long-term stability

of the nickel coating by holding the current density constant at  $5 \text{ mA/cm}^2$  for 27 h (Fig. 3.3A). This stability test shows a reasonably stable response with the small progressive increase in current likely due to evaporation of the electrolyte over the timescale of the experiment. The electroplated nickel coating also showed no visible evidence of degradation or delamination. The thickness of the nickel film estimated by measuring the charge passed through the cathodic peak at  $\sim 1.3 \text{ V}$  (Fig. 3.3B).<sup>111,112</sup> The thickness of the redox-active oxyhydroxide layer was estimated to be  $\sim 19 \text{ nm}$  during the first cycle and  $\sim 30 \text{ nm}$  during the tenth cycle (the density of the films was estimated to be  $4.1 \text{ g cm}^{-3}$ ). These collective results confirmed the viability of depositing an electrocatalytic layer of nickel on 3D-printed PLA.



**Figure 3.3** (A) First and tenth cyclic voltammogram cycles recorded ( $\nu = 10 \text{ mV s}^{-1}$ ) on planar Ni:PLA (red) and planar PLA (orange). Inset: Chronopotentiometry recorded on the planar Ni:PLA at a constant anodic current density of  $4 \text{ mA cm}^{-2}$ . (B) The cathodic charge passed over the first 10 cyclic voltammetry sweeps conducted on a planar Ni:PLA electrode. Electrochemistry conditions: counter electrode = nickel foam; reference electrode = Ag/AgCl, KCl (sat'd); electrolyte = 1.0 M KOH (aq); cyclic voltammogram scan rate =  $10 \text{ mV s}^{-1}$ . Data not corrected for uncompensated resistance.



### 3.2.2 3D-Printed Plastic Flow-Field Plates

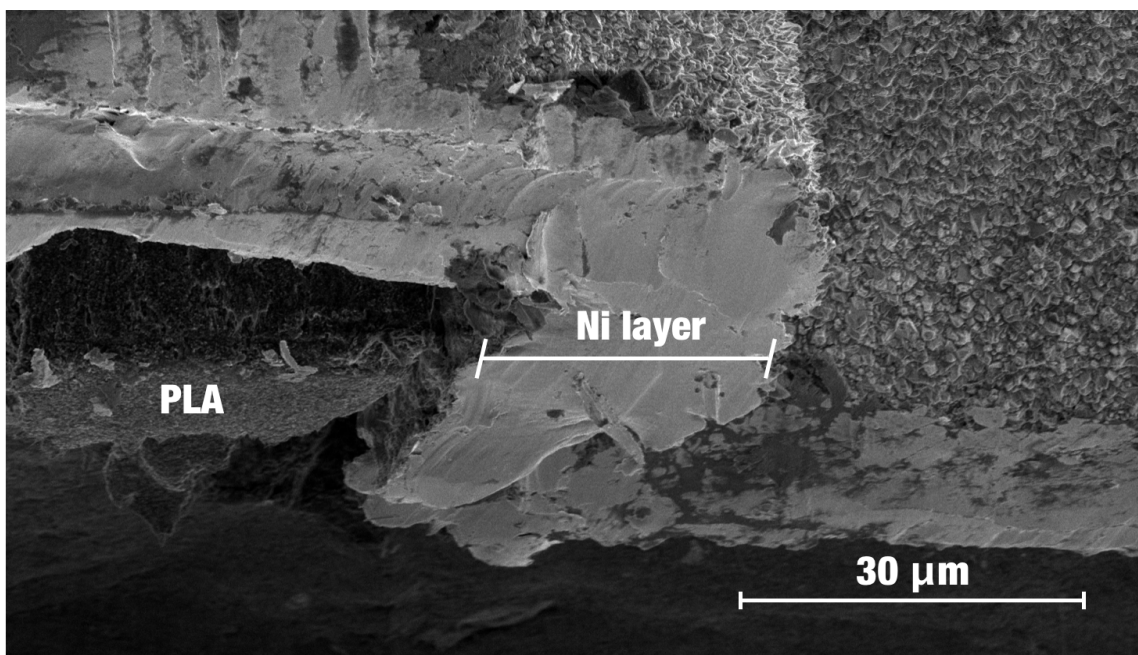
The next stage of our experiments was to design a 3D-printed flow-field plate that could be used in our electrolyzer test cell. There are many different geometries for electrolyzer flow-field plates to distribute liquid phase reactants and gas phase products with minimal pressure drop.<sup>113</sup> The rapid prototyping of different flow-field plates would therefore be hugely beneficial given the number of parameters that can be modified (e.g., rib width, channel depth, geometric configuration) but currently do not exist. We contend that 3D-printing provides access to cost-effectively and rapidly investigating different flow-field plate geometries.<sup>107</sup> This claim is supported by our ability to make three flow-field plates with different geometries common to electrolyzers (Fig. 3.4), each designed to be easily interchangeable within a single electrolyzer housing (Fig. 3.1).



**Figure 3.4** 3D-printed flow-field plates with three different flow-field patterns.

The serpentine flow-field plate containing channels 0.1 cm wide and 0.1 cm deep (Fig. 3.1) was selected as the superior architecture and used for electroplating and catalytic testing.

The deposition of uniform nickel coatings on the complex geometry was carried out in counter-electrode cage formed from expanded nickel mesh fixed in the Watt's electroplating bath so that the flow-field plate (working electrode) and the mesh were separated by <3.0 mm to promote a uniform electric field around the flow-field plate during electroplating. The electroplating was carried out on the flow-field plate by holding a cathodic current density of  $2.5 \text{ mA cm}^{-2}$  for a total of 8 h. The resultant nickel-coated PLA plate (**Ni:PLA**) was cut with a razor and imaged using a SEM to confirm a uniform coating  $\sim 25 \text{ }\mu\text{m}$  thick (Fig. 3.5). This thickness is consonant with the plating thickness of  $24.6 \text{ }\mu\text{m}$  estimated from the charge passed during the electrodeposition process. Moreover, the mass ratio of **Ni/Ni:PLA** was measured to be approximately 7, which is in strikingly close agreement with the value predicted from the analysis presented in Table 3.1.



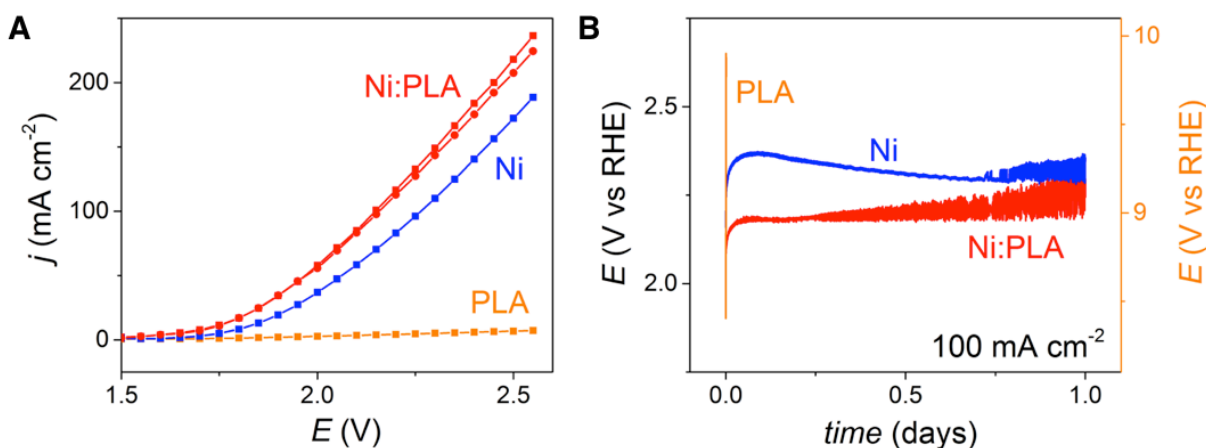
**Figure 3.5** High-angle cross sectional SEM of an electroplated nickel layer on a PLA flow-field plate.

### 3.2.3 Electrocatalysis with Plastic Flow-Field Plates

A proof-of-concept electrolyzer cell was built in-house and consists of 3D-printed flow-field housing, 3D-printed interchangeable flow-field plates and a MEA was assembled to evaluate the electrocatalytic behavior of **Ni:PLA**. The reusable flow-field housing was 3D-printed from a non-conductive ABS plastic, and a titanium busbar was used to interlock the interchangeable flow-field plate to the reusable housing and provide a contact to an external circuit. The MEA consists of Ni foam anode and cathode gas diffusion layers hot-pressed onto a Zirfon™ Perl UTP separator membrane.<sup>100</sup> The MEA was exchanged before each long-term electrochemical test so degradation of the MEA components could be distinguishable from degradation of the flow-field

plates. The electrolyte solution containing 1.0 M KOH was pumped through the cell using two peristaltic pumps at a flow rate of 4.0 mL min<sup>-1</sup>.

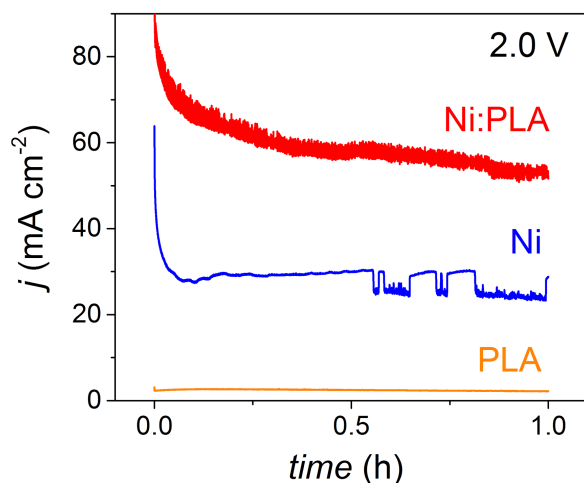
A series of electrochemical tests were recorded on cells containing serpentine flow-field plates with uniform geometries but differed in the material from which they were constructed (Fig. 3.6). The three types of plates with uniform dimensions tested here were the 3D-printed conductive PLA electroplated with nickel (**Ni:PLA**) and two flow-field plates used as controls: Machined Nickel 200 alloy (**Ni**); and 3D-printed conductive PLA (**PLA**).



**Figure 3.6** 3D-printed electrolyzer test cell performance. (A) Staircase voltammetry recorded on electrolyzer cells with flow-field plates made of bulk Nickel 200 alloy (*blue*), conductive PLA (*orange*), nickel electroplated PLA (*red with squares*), and nickel electroplated PLA after >100 h of electrolyzer operation (*red with circles*). (B) Chronopotentiometry recorded on electrolyzer cells with flow-field plates made of bulk Nickel 200 (*blue*), carbon PLA (*orange*), and nickel electroplated PLA (*red*) at a held current density of 100 mA cm<sup>-2</sup>. Electrochemistry conditions: 1.0 M KOH<sub>(aq)</sub>; staircase voltammogram sample width = 30 s; staircase voltammogram sample period = 50 s. Data not corrected for ohmic resistance.

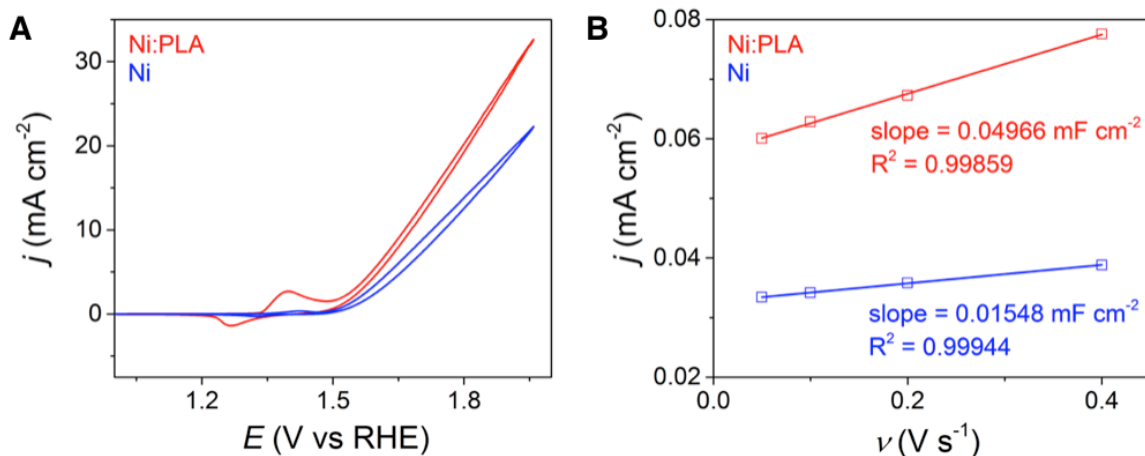
Stair-case voltammetry (0.05-V steps from 0 to 2.6 V) measured on cells containing **Ni** showed a progressively increasing current as the voltage was swept to potentials higher than 1.5 V consistent with electrocatalysis. The same measurements on **Ni:PLA** yielded nearly superimposable to that of the **Ni** cells, while **PLA** produced nominal current over this same range. This data taken together is consistent with electrolysis occurring at the **Ni:PLA** substrate, with little current arising from the decomposition of the plastic on the time-scale of the experiment.

Chronopotentiometry experiments performed on cells with the control **Ni** flow-field plate required an applied potential of  $\sim 2.3$  V to achieve a constant current density of  $100 \text{ mA cm}^{-2}$  over 1 day of experiments. (The increasing level of noise in the data collection over the course of the experiments which may be due to build-up of bubbles in our apparatus.) The same experiment with **Ni:PLA** required a lower applied potential ( $\sim 2.20$  V) to achieve  $100 \text{ mA cm}^{-2}$ , but this data slightly increased with time. The **PLA** plate was not capable of electrolysis at  $100 \text{ mA cm}^{-2}$ , even with a significant applied bias of 10 V. Chronoamperometry experiments held at an external bias of 2.0 V on cells with the different flow plates yielded similar results (Fig. 3.7). The **Ni** flow-field plates produced a steady current density of  $\sim 30 \text{ mA cm}^{-2}$  (the anomalous 5-10  $\text{mA cm}^{-2}$  reductions and recoveries observed at  $>0.5$  days is again attributed to the confinement of gas bubbles). Data recorded on **Ni:PLA** resulted in current densities that stabilize at a substantially higher value of  $\sim 50 \text{ mA cm}^{-2}$ . The same experiment using the **PLA** control resulted in current densities  $<5 \text{ mA cm}^{-2}$ .



**Figure 3.7** Chronoamperometry recorded on electrolyzer cells with flow-field plates made of bulk **Ni** (*blue*), carbon **PLA** (*orange*), and nickel electroplated **Ni:PLA** (*red*). Electrochemistry conditions: applied potential = 2.0 V; electrolyte = 1.0 M KOH(aq).

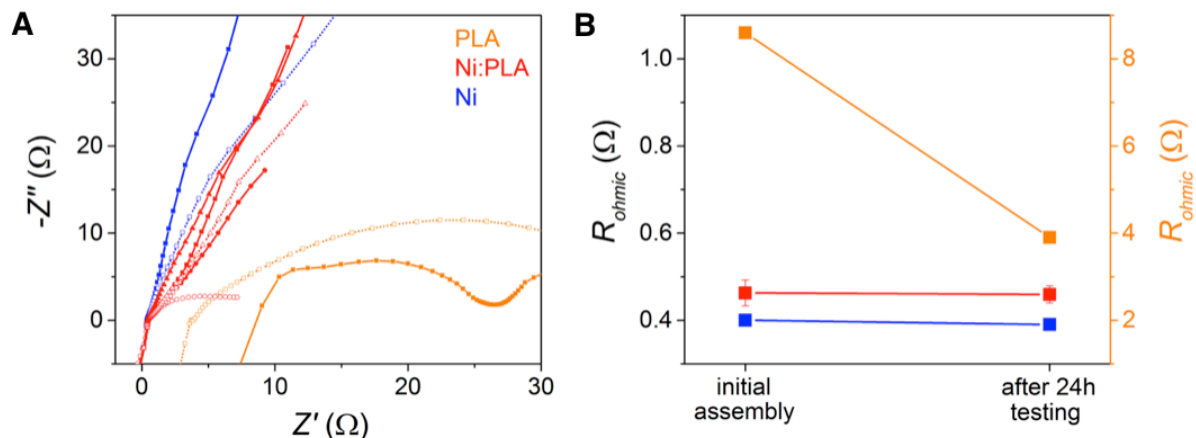
The superior performance of the cells with the **Ni:PLA** plates relative to the **Ni** plates was not expected but can be rationalized by the nature of the metal surface. The metal surface in the **Ni** flow-field plate needs to be converted to the more active nickel oxyhydroxide phase during electrolysis before it can achieve the activity of the electrodeposited layer for the **Ni:PLA** plate.<sup>111,112,114-117</sup> The accessible electrochemical surface area of the rough, porous nickel layer for **Ni:PLA** will also be inherently higher than the smooth, dense surfaces of the **Ni** plates. This is supported by independent double-layer capacitance measurements of the plates in a 3-electrode set-up, as well as the higher anodic peak at 1.4 V for the **Ni:PLA** flow-field plate (Fig. 3.8).



**Figure 3.8** (A) First cyclic voltammogram cycle recorded on a **Ni:PLA** flow-field plate (*red*) and a **Ni** flow-field plate (*blue*) in a 3-electrode cell. (B) Cyclic voltammograms were measured in a non-Faradaic region of the voltammogram at the following scan rate: 0.05, 0.1, 0.2, and 0.4 V/s. All current is assumed to be due to capacitive charging. Electrochemistry conditions: counter electrode = nickel foam; reference electrode = Ag/AgCl, KCl (sat'd); electrolyte = 1.0 M KOH (aq); cyclic voltammogram scan rate = 10 mV s<sup>-1</sup>. Data not corrected for uncompensated resistance.

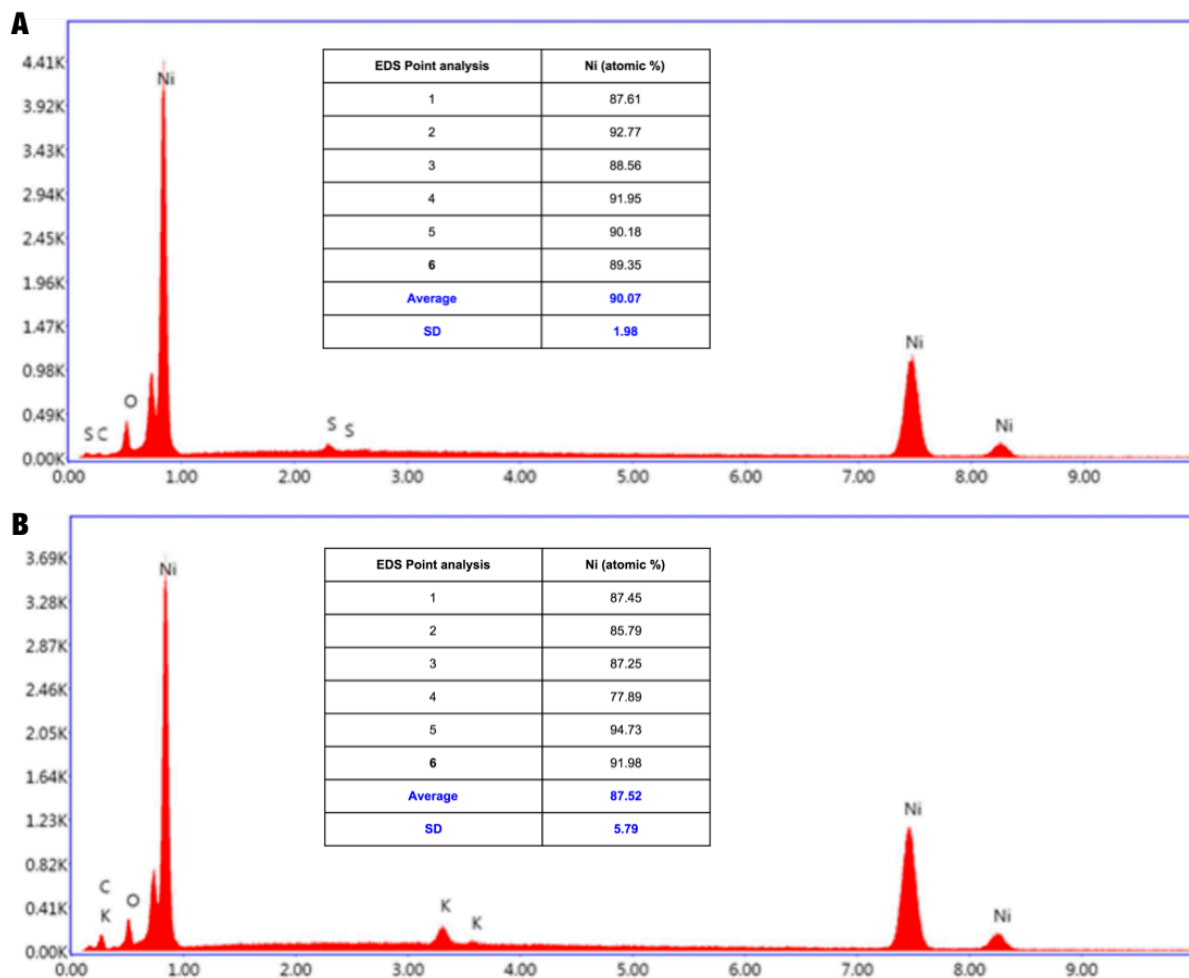
The ohmic cell resistance determined by electrochemical impedance spectroscopy (EIS) of the electrolyzer cell assembly (Fig. 3.9) before and after 24 h of sustained electrolysis ruled out differences in ohmic cell resistances being responsible for the differences in catalytic activity (**Ni** = 0.405  $\Omega$ ; **Ni:PLA** = 0.469  $\Omega$ ). The cell containing the **PLA** plate had an ohmic resistance (> 8  $\Omega$ ) too high to expect electrocatalysis, thus confirming the need for a conductive coating on the plastic flow-field plate (Fig. 3.6) in order for the electrolyzer to operate at commercially relevant current densities (>200 mA cm<sup>-2</sup>). We do not claim here that the **Ni:PLA** flow plate will be stable for the time periods necessary for commercial applications, but this proof-of-principle does confirm that electrolysis can occur at electroplated 3D-printed plastic substrates on the

timescale of days. The stability of the cells on these short time periods was further supported by energy-dispersive X-ray spectroscopy (EDS) analyses (Fig. 3.10) and SEM images (Fig. 3.11) that indicate the Ni present on the **Ni:PLA** flow-field plate stayed constant before and after 24 h of chronopotentiometry and 24 h chronoamperometry.

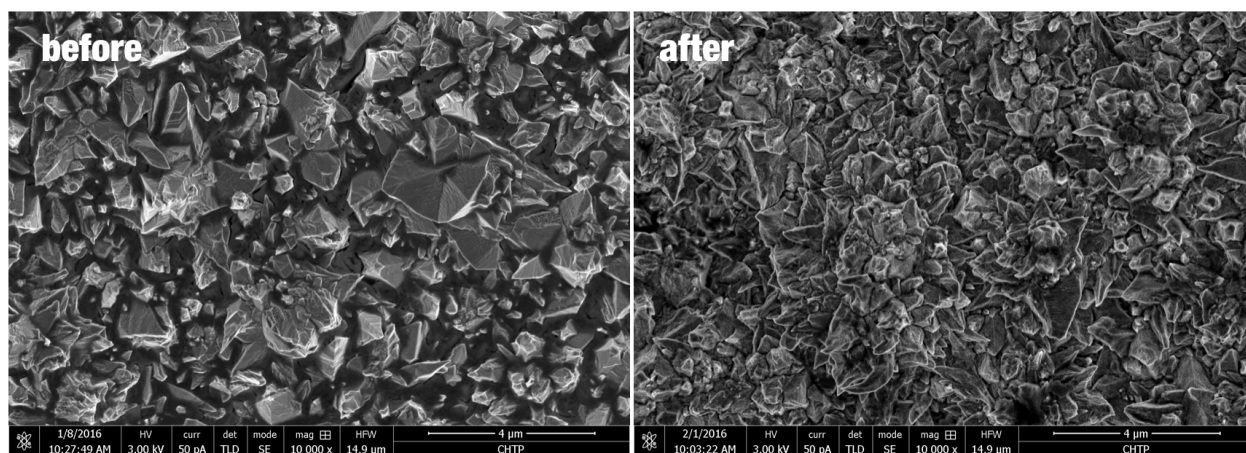


**Figure 3.9** Alternating current electrochemical impedance spectroscopy (EIS) recorded on electrolyzers with different flow-field materials. (A) Nyquist plots of EIS recorded on electrolyzer cells with flow-field plates made of bulk Nickel 200 alloy (*blue*), conductive PLA (*orange*), nickel electroplated PLA (*red*). Solid lines indicate data recorded before electrolysis experiments, dashed lines indicate data recorded after 24 h testing. Three different examples of data recorded on **Ni:PLA** are shown. All EIS was recorded at open cell potential (OCP). (B) Ohmic cell resistances extrapolated from electrochemical impedance spectra recorded on electrolyzer cells with flow-field plates made of bulk **Ni** 200 alloy (*blue*), conductive **PLA** (*orange*), nickel electroplated **Ni:PLA** (*red*).





**Figure 3.10** Elemental analysis of six different points on the central flow-field rib (fifth rib from top) using energy-dispersive x-ray spectroscopy. Representative EDS spectrum: x-axes = energy (keV); y-axes = intensity (counts). **(A)** Before electrolysis. **(B)** After 24 h chronoamperometry and 24 h chronopotentiometry.



**Figure 3.11** SEM image of an electroplated nickel layer on a PLA flow-field plate before and after 48 h of electrolysis.

### 3.3 Summary

This chapter reports a demonstration of electroplating of metal directly on a 3D-printed plastic without the need of a seeding layer. This achievement leaves open the possibility of a significant reduction in the metal that comprises many commercial components. This chapter highlights how the metal flow-field plates used in electrolyzers can be potentially replaced by electroplated 3D-plastic components with similar dimensions. The weight of the Ni:PLA flow-field plates evaluated in this study were measured to be reduced by 7-fold, respectively. The markedly large reduction in weight could ease the production, transportation, and handling of electrolyzer stacks, as well as reduce material costs. Moreover, 3D-printing of these components can replace computerized numerical-control milling of pure metallic components to increase the speed and lower the costs of prototyping such components. The interchangeable flow-field feature will be used for the optimization of flow-field designs in future studies.

### **3.4 Methods**

#### **3.4.1 Materials**

Nickel (II) sulfate hexahydrate ( $\text{NiSO}_4 \cdot 6 \text{H}_2\text{O}$ ), nickel (II) chloride hexahydrate ( $\text{NiCl}_2 \cdot 6 \text{H}_2\text{O}$ ), and boric acid ( $\text{H}_3\text{BO}_3$ ) were purchased from Strem Chemicals. Potassium Hydroxide (KOH) pellets were purchased from Sigma-Aldrich. Reagents were used as received and without further purification. Zirfon Perl UTP 500 membranes were sourced from AGFA. Nickel foam gas diffusion electrode material was purchased from MTI. Ni expanded mesh was purchased from Dexmet Corporation. The PLA filament with added carbon black (1.75 mm diameter “Conductive PLA” by Protoplant) was purchased from Proto-Pasta. ABS filament (1.75 mm “Natural ABS” by MatterHackers) was purchased from MatterHackers. Filaments were used as received. Nickel 200 sheet with 0.25 in thickness was purchased from onlinemetals.com.

#### **3.4.2 3D-printing**

A Rostock MAX v2 desktop 3D-Printer from SeeMeCNC running Repetier 0.91 was used to print the flow-field plate and base components. The printer’s stock hot end was replaced with an E3D-v6 with a 0.4 mm nozzle. Mattercontrol 1.2.2 for Mac (Rostock MAX v2 preconfiguration) was downloaded from [www.seemecnc.com](http://www.seemecnc.com) and used to control the printer. Prints were sliced with the MatterSlice engine. Flow-field plates were printed with 100% infill, and oriented such that print layers are perpendicular to the raised flow-field plate ribs. Conductive PLA was printed with an extruder temperature of 230 °C and heated bed temperature of 60 °C onto a layer of Kapton tape applied to the print bed. ABS was printed with an extruder temperature of 237 °C and a heated bed temperature of 85 °C onto a fresh coating of UHU glue

stick applied to the print bed. Flow-fields and bases were designed using SolidWorks 2013 software.

### 3.4.3 Electrode Preparation and Ni Electroplating

The PLA electrode with planar geometry was a 3D-printed cuboid ( $2.0\text{ cm} \times 1.0\text{ cm} \times 0.2\text{ cm}$ ) with a removable clip ( $0.5\text{ cm} \times 0.5\text{ cm} \times 0.1\text{ cm}$ ) on the top face. A serpentine design was chosen for flow-field testing. The 3D-printed flow-fields were  $2.4\text{ cm} \times 2.4\text{ cm} \times 0.5\text{ cm}$  with a wetted active area of  $4.0\text{ cm}^2$ . The flow-field channels had a width of 1.1 mm, flow-field ribs had a width of 1.3 mm and a height of 1.2 mm. An additional removable clip ( $1.1\text{ cm} \times 0.4\text{ cm} \times 0.2\text{ cm}$ ) on the top rectangular face was included to attach an alligator clip during electroplating. Prior to Nickel electrodeposition, all 3D-printed electrodes and flow-field plates were cleaned by sonication in 1.0 M HCl for 5 min.

A “Watts” nickel electroplating bath was prepared by adding 27.1 g of  $\text{NiSO}_4 \cdot 6\text{H}_2\text{O}$ , 5.4 g of  $\text{NiCl}_2 \cdot 6\text{H}_2\text{O}$ , and 3.6 g of  $\text{H}_3\text{BO}_3$  to 90 mL of deionized water. The pH of prepared solution was 3.47. The desired pH for electrodeposition was found to be in the range of 3.4 - 3.6 using a Fisher Scientific Accumet AB150 pH meter. The pH of the nickel bath increased during electroplating due to hydrogen evolution, therefore after each electroplating period the pH of the bath was adjusted by adding 1.0 M  $\text{H}_2\text{SO}_4$  dropwise until pH was within the desired range. A nickel counter electrode cage was fashioned from Ni expanded mesh and positioned 1.0 - 3.0 mm from all submerged outside faces of the 3D-printed object. A held cathodic current density of  $2.5\text{ mA cm}^{-2}$  of submerged surface area was used for electroplating nickel onto 3D-printed objects, using a Keithley 2231A-30-3 triple channel DC power supply. The conductive PLA electrode

with planar geometry had a submerged surface area of 5.0 cm<sup>2</sup> ( $I_{\text{electrodeposition}} = 13 \text{ mA}$ ).

Electroplating of conductive PLA electrodes with a planar geometries was performed by holding a cathodic current for two periods of 2 h for a total electroplating time of 4 h. After each 2 h period, the current was stopped and the pH was adjusted to the desired range before the second 2-h electroplating period was initiated. Flow-field plates had a submerged surface area of 20.4 cm<sup>2</sup> ( $I_{\text{electrodeposition}} = 51 \text{ mA}$ ). Electroplating of flow-field plates was performed by holding a cathodic current for 4 periods of 2 h for a total electroplating time of 8 h. After each 2 h period the current was stopped and the pH was adjusted to the desired range before the next 2 h electroplating period was initiated. The thickness of the Ni coating applied during electroplating was approximated using the following formula<sup>118</sup>:

$$T = \frac{12.29It}{A} \quad (\text{Eq. 11})$$

where:  $T$  is thickness in micrometres ( $\mu\text{m}$ );  $I$  is current in amperes (A);  $t$  is time in h; and  $A$  is the submerged surface area in square decimetres (dm<sup>2</sup>).

#### 3.4.4 MEA Preparation

Nickel foam gas diffusion layers were cut into 2.5 cm × 2.5 cm squares with geometric surface area of 6.3 cm<sup>2</sup> and were sonicated in acetone for 5 min. The nickel foam was then etched by sonication in 1.0 M H<sub>2</sub>SO<sub>4</sub> for 5 min. Substrates were washed with DI water and sonicated in DI water for 5 min. Zirfon™ Perl UTP membranes were cut into 2.8 cm × 2.8 cm squares with geometric surface areas of 7.8 cm<sup>2</sup>. Membrane electrode assemblies were hot-

pressed using a Dake hot-press model 44226 at 125 °C and 400 psi for 3 min. MEAs were hydrated in 1.0 M KOH for at least 24 h after hot-pressing.

### 3.4.5 Physical Methods

Electrochemical data recorded using a C-H Instruments Workstation 660D potentiostat with amp booster. Cyclic voltammograms and chronopotentiometry were recorded on a PLA electrode and a Ni-plated PLA electrode with planar geometry in a three-electrode h-cell setup with a Ni Foam counter electrode and a Ag/AgCl (sat. KCl) reference electrode. The Ag/AgCl (sat. KCl) reference electrode was calibrated in H<sub>2</sub> saturated 1.0 M KOH using Pt disk electrodes as the working and counter electrode. Cyclic voltammograms were acquired at a 10 mV s<sup>-1</sup> scan rate. No aggregation was induced on the test cell besides that from evolved gaseous products. Cyclic voltammetry were recorded on **Ni** (half submerged, geometric surface area of 13.1 cm<sup>2</sup>) and **Ni:PLA** (half submerged, geometric surface area of 10.67 cm<sup>2</sup>) in a custom three-electrode setup with a Ni foam counter electrode and a Ag/AgCl (sat. KCl) reference electrode. The Ag/AgCl (sat. KCl) reference electrode was calibrated in H<sub>2</sub> saturated 1.0 M KOH using Pt disk electrodes as the working and counter electrode. Data was acquired at a 10 mV s<sup>-1</sup> scan rate. Reported potentials were not corrected for uncompensated resistance (*iR*). No aggravation was induced on the test cell besides that from evolved gaseous products.

Electrolyzer polarization, chronopotentiometry, chronoamperometry, alternating current electrochemical impedance spectroscopy (EIS) data were recorded in a two-electrode setup. The alligator clips from the potentiostat were clipped to titanium bus bars designed to insert into the flow-fields. The anode bus bar had the working electrode alligator clip attached and the cathode

bus bar had the reference and counter electrode alligator clip attached. The flow-rate through the flow-field channels was  $4 \text{ ml min}^{-1}$  at the anode and cathode. An o-ring is used to create a seal between the MEA and the outside of the flow-field plate, while compression between the two housing halves is provided by four firmly hand tightened bolts. 1.0 M KOH electrolyte was circulated at a rate of  $4 \text{ mL min}^{-1}$  using dual peristaltic pumps (Fig. S4). Polarization data recorded as staircase voltammetry: sample width = 30 s; sample period = 50 s. EIS data were recorded at open circuit potential between 1 and 10000 Hz with a potential amplitude of 0.005 V. Cell resistance was taken as the x-intercept of the Nyquist plot or the value of  $Z'$  at  $-Z'' = 0 \Omega$ . The output electrolyte was filtered through Whatman<sup>TM</sup> (Cat. No. 1001 090) filter papers before being recycled through the electrolyzer via a 500 mL reservoir (Fig. S4).

Field emission scanning electron microscopy (FE-SEM) and energy-dispersive X-ray spectroscopy (EDS) data was acquired with a FEI Helios NanoLab 650 microscope. FE-SEM imaging was performed in secondary electron mode (voltage: 3kV, current: 50 pA, Everhart-Thornley and Elstar in-lens secondary electron detectors) and EDX analysis was carried out at 15 kV and 3.2 nA.

#### **3.4.6 Flow-Plate Techno-Economic Analysis**

A hypothetical zero-gap bipolar flow-field plate ( $25 \text{ cm}^2$ ) and alkaline bipolar plate ( $2500 \text{ cm}^2$ ) were used for the economic analysis found in Table 3.1. Zero material waste was assumed (i.e., 100% of the waste produced during milling of flow-field channels is recoverable) and both plates were assumed to be 0.3 cm thick. The volumetric prices and densities for all flow-field plate materials were based on values from the sources indicated in (Table 3.3). For a  $25 \text{ cm}^2$

bipolar flow-field plate, there would be 25 ribs (0.1 cm width, 0.1 cm depth) and channels (0.1 cm width). For one rib + channel the electroplated surface area ( $4 \text{ cm}^2$ ) was determined by multiplying the electroplated perimeter of a rib + channel (0.8 cm) and flow-field plate side length (5 cm). The surface area of the perimeter sides of the flow-field plate ( $0.3 \text{ cm} \times 5 \text{ cm} \times 4$  sides) was added to the total surface area of ribs and channels ( $100 \text{ cm}^2$ ) to give the total electroplated surface area ( $106 \text{ cm}^2$ ). The total electroplated surface area was multiplied by the thickness of the Ni coating ( $25 \text{ }\mu\text{m}$ ) to determine the volume ( $0.265 \text{ cm}^3$ ) and mass (2.35 g) of nickel added to the bipolar flow-field plate. One-third of the volume of a square slab of material ( $0.3 \text{ cm} \times 25 \text{ cm}^2$ ) is removed to create the channels for a bipolar flow-field plate resulting in a channeled flow-field plate of  $5 \text{ cm}^3$  volume in this example. Density and volumetric cost data were used to tabulate the mass and cost of flow-field plates of different materials (Table 3.4). For a an alkaline electrolyzer a circular cross sectional area of  $2500 \text{ cm}^2$  and a plate thickness of 0.3 cm was assumed. The total surface area of the plate ( $2 \times 2500 \text{ cm}^2 + 53.2 \text{ cm}^2$ ) was multiplied by the thickness of the Ni coating ( $25 \text{ }\mu\text{m}$ ) to determine the volume ( $12.6 \text{ cm}^3$ ) and mass (111.9 g) of nickel added by electroplating. The volume of material used in an alkaline electrolyzer flow-field plate ( $750 \text{ cm}^3$ ) was used with density and volumetric material cost to tabulate the cost of flow-field plates made from different materials (Table 3.4).



**Table 3.3** Relative prices and densities of flow-field plate materials.

material	volumetric pricing (US\$ cm <sup>-3</sup> )	density (g cm <sup>-3</sup> )	source
titanium (grade 2)	0.316	4.51	McMaster-Carr
graphite (high conductivity)	0.155	1.70 <sup>a</sup>	McMaster-Carr
stainless steel (corrosion resistant)	0.260	7.75	McMaster-Carr
nickel (corrosion resistant)	0.196	8.86	McMaster-Carr
conductive PLA (filament)	0.101	1.15	Proto-pasta
ABS (filament)	0.031	1.01	MatterHackers

<sup>a</sup>Measured**Table 3.4** Techno-economic analysis of electrolyzer bipolar plates

material	zero-gap				conventional			
	actual		relative		actual		relative	
	mass (g)	cost (\$)	mass	cost	mass (kg)	cost (\$)	mass	cost
Nickel	44.3	0.98	5.5	1.8	6.6	147.0	6.8	1.9
Stainless Steel	38.8	1.30	4.8	2.3	5.8	195.0	6.0	2.5
Titanium	22.6	1.58	2.8	2.8	3.4	237.0	3.5	3.0
Conductive PLA	5.75	0.51	-	-	0.86	75.8	-	-
Ni:PLA <sup>a</sup>	8.10	0.56	1.0	1.0	0.97	78.2	1.0	1.0

<sup>a</sup>Electrodeposited nickel was assumed to have the same volumetric cost and density as bulk nickel.

## Chapter 4: Conclusion

### 4.1 Conclusion

Metals used as electrocatalysts and flow-field plates contribute a significant percentage of the capital cost of electrolyzer stacks. High capital costs undermine the commercial application of smaller sized electrolyzers and experimental designs. This thesis highlights two distinctive methods to reduce the metal content of low temperature water electrolyzers.

#### 4.1.1 Amorphous Catalyst Coated Membranes

The first strategy explored in this thesis was a method for incorporating photodeposited amorphous electrocatalyst thin films that mediate the OER into a MEA for PEM electrolyzers. UVDD was employed to deposit an  $\alpha$ -IrO<sub>x</sub> film on a non-conductive and hydrophobic substrate that was then used in a decal transfer procedure that formed the CCM. The activity of the resulting CCM towards the OER was comparable with other amorphous iridium oxide thin films in the literature, demonstrating a current density of 10 mA/cm<sup>2</sup> at an overpotential of ~400 mV during cyclic voltammetry experiments. The low catalyst loading of 0.03 mg cm<sup>-2</sup> ( $\sigma$  = 0.01 mg cm<sup>-2</sup>) of  $\alpha$ -IrO<sub>x</sub> CCMs produced during this thesis was initially attributed to the low current densities, however, the Millet group has recently demonstrated a PEM electrolyzer with 0.1 mg/cm<sup>2</sup> IrO<sub>2</sub> that reached 1 mA/cm<sup>2</sup> at a cell voltage of 1.9 V,<sup>80</sup> revealing that further optimization is needed for use of amorphous films in PEM electrolyzers. The crystalline IrO<sub>2</sub> nanoparticles and ionomer used for Millet's study are most likely resulting in a more porous catalyst layer with a greater amount of triple-phase boundary reaction sites. Furthermore, the

cell used in their study facilitated fluid flow at  $\sim 3.3 \text{ mL min}^{-1}$ , where the cell used in our study had zero agitation, giving their cell less of a mass transport limitation.

#### **4.1.2 Nickel-plated, 3D-printed Plastic Electrolyzer Components**

The second method explored in this thesis involved incorporating plastic electrodes in an alkaline electrolyzer to reduce capital and manufacturing costs. Electroplating a nickel coating on 3D-printed carbon infused polylactic acid plastic enabled the use of low cost and low density plastic flow-field plate materials in alkaline media. This method is an example of electroplating on 3D-printed plastics without the need for a seeding layer and can enabled facile manufacturing of lab-scale electrolyzers and nickel-plated electrolyzer flow-fields. These flow-fields provided stable conductivity to the plastic electrolyzer device. The replacement of heavy and relatively expensive metallic components with plastics would reduce the capital cost and manufacturing cost of electrolyzers. The utility of using plastic nickel-plated flow-field plates was demonstrated by using MEAs comprised of nickel foam gas diffusion electrodes and Zirfon membranes. The electrolyzer reached low current densities compared to more optimized AEM devices reported in literature, however, the electrolyzer tested in this thesis performed better with flow-field plates made of nickel-plated PLA (**Ni:PLA**) than with flow-field plates formed from machined nickel at commercially relevant current densities ( $200 \text{ mA cm}^{-2}$ ) at room temperature.

## **4.2 Future Directions**

### **4.2.1 Amorphous Catalyst-coated Membranes**

Amorphous iridium oxide and Nafion membranes were chosen for this preliminary study because they are ubiquitous in PEM electrolyzers. The CCMs we produced, however, did not achieve commercially relevant and thus, further experimental optimization is needed. The performance of the amorphous catalyst-coated membranes could be improved by loading the catalyst layer ( $\sim 0.1 \text{ mg cm}^{-1}$ ) without limiting proton and water transport through the catalyst layer. In previous studies, proton exchange ionomers were employed to build up the catalyst-loading without impeding the transport of water and protons.<sup>29</sup> Optimization of the CCMs produced from UVDD/decal transfer can be accomplished by incorporating Nafion ionomer in the amorphous metal oxide film. This could possibly be accomplished by layered deposition of  $\alpha\text{-IrO}_x$  and ionomer on the membrane. The technique still is also useful for the production of components for other electrochemical applications, such as electrochromic devices or photoelectrochemical devices, where thin films of metal oxides are interfaced with solid polymer electrolytes or non-conductive substrates.

### **4.2.2 Electroplating on Commercial-Sized Electrolyzer Flow-Field Plates.**

Using plastic components to manufacture electrolyzers promises to improve the scalability of the technology by reducing weight, manufacturing time, and capital costs of the device. Electroplating of  $>25 \text{ }\mu\text{m}$  nickel coatings must be achieved on large, commercial-sized electrolyzer bipolar plates if the method highlighted in *Chapter 3* will prove useful for prototyping alkaline electrolyzer flow-plate materials. Furthermore, optimization is needed in

terms of understanding the gas tightness of the **Ni:PLA** flow-field plates, as well as operation at higher temperatures and pressures.

Previously, a myriad of flow-field designs have been tested and modelled in an effort to optimize flow-field design used in PEM fuel cells;<sup>113,119,120</sup> however, the flow dynamics in electrolyzer flow-fields will differ from that in fuel cells. The optimization of a flow-field design is a balance between reactant distribution and pressure drop. For example, the interdigitated design is optimal for reactant distribution in the MEA and the parallel design causes very little pressure drop, reducing pumping costs. The serpentine design strikes a balance of pressure drop in the flow-field and product distribution in the MEA. Moreover, a large variety of hybrid designs are possible that may increase electrolyzer performance. The plastic electrolyzer test cell highlighted in this thesis, designed to incorporate interchangeable flow-fields, can be used to rapidly test different hybrid designs and will serve to accelerate flow-field design optimization for electrolyzers, lending itself well to the rapid prototyping.

## References

- (1) Lewis, N. S.; Nocera, D. G. *Proceedings of the National Academy of Sciences* **2006**, *103*, 15729–15735.
- (2) Bolton, J. R.; Hall, D. O. *Annual Review of Energy*, *4*, **1979**.
- (3) Service, R. F. *Science* **2015**, *309*, 548–551.
- (4) Armaroli, N.; Balzani, V. *Angew. Chem. Int. Ed.* **2007**, *46*, 52–66.
- (5) Gust, D.; Moore, T. A.; Moore, A. L. *Acc. Chem. Res.* **2009**, *42*, 1890–1898.
- (6) Mergel, J.; Carmo, M.; Fritz, D. In *Transition to Renewable Energy Systems*; Stolten, D.; Scherer, V., Eds.; Wiley-VCH, 2013.
- (7) Katsounaros, I.; Cherevko, S.; Zeradjanin, A. R.; Mayrhofer, K. J. J. *Angew. Chem. Int. Ed.* **2013**, *53*, 102–121.
- (8) Gray, H. B. *Nature Chemistry* **2009**, *1*, 7–8.
- (9) Nocera, D. G. *Acc. Chem. Res.* **2012**, *45*, 767–776.
- (10) Shapiro, D.; Duffy, J.; Kimble, M.; Pien, M. *Solar Energy* **2005**, *79*, 544–550.
- (11) Herzog, A.; Tatsutani, M. *A HYDROGEN FUTURE?*; Natural Resources Defense Council, 2005; pp. 1–23.
- (12) Sørensen, B. *Hydrogen and Fuel Cells: Emerging Technologies and Applications*; Academic Press: Burlington, MA, 2005.
- (13) Pinaud, B. A.; Benck, J. D.; Seitz, L. C.; Forman, A. J.; Chen, Z.; Deutsch, T. G.; James, B. D.; Baum, K. N.; Baum, G. N.; Ardo, S.; Wang, H.; Miller, E.; Jaramillo, T. F. *Energy & Environmental Science* **2013**, *6*, 1983.
- (14) Maniyali, Y.; Almansoori, A.; Fowler, M.; Elkamel, A. *Ind. Eng. Chem. Res.* **2013**, *52*, 7470–7481.
- (15) Turner, J. A. *Science* **2004**, *305*, 972–974.
- (16) Ball, M.; Weeda, M. *International Journal of Hydrogen Energy* **2015**, *40*, 7903–7919.
- (17) Marchenko, O. V.; Solomin, S. V. *International Journal of Hydrogen Energy* **2015**, *40*, 3801–3805.
- (18) Schaub, G.; Eilers, H.; González, M. I. In *Transition to Renewable Energy Systems*; Stolten, D.; Scherer, V., Eds.; Wiley-VCH, 2013.
- (19) Djafour, A.; Matoug, M.; Bouras, H.; Bouchekima, B.; Aida, M. S.; Azoui, B. *International Journal of Hydrogen Energy* **2011**, *36*, 4117–4124.
- (20) Ghosh, P. C.; Emonts, B.; Janßen, H.; Mergel, J.; Stolten, D. *Solar Energy* **2003**, *75*, 469–478.
- (21) Barbir, F. *Solar Energy* **2005**, *78*, 661–669.
- (22) Qadrdan, M.; Abeysekera, M.; Chaudry, M.; Wu, J.; Jenkins, N. *International Journal of Hydrogen Energy* **2015**, *40*, 5763–5775.
- (23) Kang, J. E.; Brown, T.; Recker, W. W.; Samuelsen, G. S. *International Journal of Hydrogen Energy* **2014**, *39*, 3444–3449.
- (24) Yang, Z.; Zhang, G.; Lin, B. *International Journal of Hydrogen Energy* **2015**, 1–10.
- (25) Su, Z.; Ding, S.; Gan, Z.; Yang, X. *International Journal of Hydrogen Energy* **2014**,

- 39, 7202–7215.
- (26) Sørensen, B. *Hydrogen and Fuel Cells: Emerging Technologies and Applications*; Academic Press: 2012.
  - (27) Leroy, R. L.; Bowen, C. T. *Journal of the Electrochemical Society* **1980**, *127*, 1954–1962.
  - (28) Millet, P.; Ngameni, R.; Grigoriev, S. A.; Mbemba, N.; Brisset, F.; Ranjbari, A.; Etiévant, C. *International Journal of Hydrogen Energy* **2010**, *35*, 5043–5052.
  - (29) Carmo, M.; Fritz, D. L.; Mergel, J.; Stolten, D. *International Journal of Hydrogen Energy* **2013**, *38*, 4901–4934.
  - (30) Saur, G. *Wind-to-hydrogen project: Electrolyzer capital cost study*; NREL/TP-550-44103; National Renewable Energy Laboratory, 2008; pp. 1–48.
  - (31) Varcoe, J. R.; Atanassov, P.; Dekel, D. R.; Herring, A. M.; Hickner, M. A.; Kohl, P. A.; Kucernak, A. R.; Mustain, W. E.; Nijmeijer, K.; Scott, K.; Xu, T.; Zhuang, L. *Energy & Environmental Science* **2014**, *7*, 3135–3191.
  - (32) Pavel, C. C.; Cecconi, F.; Emiliani, C.; Santuccioli, S.; Scaffidi, A.; Catanorchi, S.; Comotti, M. *Angew. Chem. Int. Ed.* **2013**, *53*, 1378–1381.
  - (33) Leng, Y.; Chen, G.; Mendoza, A. J.; Tighe, T. B.; Hickner, M. A.; Wang, C.-Y. *J. Am. Chem. Soc.* **2012**, *134*, 9054–9057.
  - (34) Xiao, L.; Zhang, S.; Pan, J.; Yang, C.; He, M.; Zhuang, L.; Lu, J. *Energy & Environmental Science* **2012**, *5*, 7869.
  - (35) Ursúa, A.; Martín, I. S.; Barrios, E. L.; Sanchis, P. *International Journal of Hydrogen Energy* **2013**, *38*, 14952–14967.
  - (36) Ganley, J. C. *International Journal of Hydrogen Energy* **2009**, *34*, 3604–3611.
  - (37) Morgan, E. R.; Manwell, J. F.; McGowan, J. G. *International Journal of Hydrogen Energy* **2013**, *38*, 15903–15909.
  - (38) Bonke, S. A.; Wiechen, M.; MacFarlane, D. R.; Spiccia, L. *Energy & Environmental Science* **2015**, 1–6.
  - (39) Ayers, K. E.; Anderson, E. B.; Capuano, C.; Carter, B. D.; Dalton, L. T.; Hanlon, G.; Manco, J.; Niedzwiecki, M. *ECS Transactions* **2010**, *33*, 3–15.
  - (40) McCrory, C. C. L.; Jung, S.; Ferrer, I. M.; Chatman, S. M.; Peters, J. C.; Jaramillo, T. F. *J. Am. Chem. Soc.* **2015**, *137*, 4347–4357.
  - (41) Li, X.; Walsh, F. C.; Pletcher, D. *Phys. Chem. Chem. Phys.* **2011**, *13*, 1162–1167.
  - (42) Lin, L.; Zhu, Q.; Xu, A.-W. *J. Am. Chem. Soc.* **2014**, *136*, 11027–11033.
  - (43) Qiu, Y.; Xin, L.; Li, W. *Langmuir* **2014**, *30*, 7893–7901.
  - (44) Ahn, S. H.; Park, H.-Y.; Choi, I.; Yoo, S. J.; Hwang, S. J.; Kim, H.-J.; Cho, E.; Yoon, C. W.; Park, H.; Son, H.; Hernandez, J. M.; Nam, S. W.; Lim, T.-H.; Kim, S.-K.; Jang, J. H. *International Journal of Hydrogen Energy* **2013**, *38*, 13493–13501.
  - (45) Sheng, W.; Bivens, A. P.; Myint, M.; Zhuang, Z.; Forest, R. V.; Fang, Q.; Chen, J. G.; Yan, Y. *Energy & Environmental Science* **2014**, *7*, 1719.
  - (46) Morales-Guio, C. G.; Liardet, L.; Mayer, M. T.; Tilley, S. D.; Grätzel, M.; Hu, X. *Angew. Chem. Int. Ed.* **2014**, *53*, 1–5.

- (47) McKone, J. R.; Marinescu, S. C.; Brunschwig, B. S. *Chemical Science* **2014**, *5*, 865–878.
- (48) Russell, J. H.; Nuttall, L. J.; Fickett, A. P. *American Chemical Society*. **1973**, 1–196.
- (49) Grubb, J. Fuel Cell. U.S. Patent 2,913,511, 1959.
- (50) Grubb, W. T.; Niedrach, L. W. *Journal of the Electrochemical Society* **1960**, *107*, 131.
- (51) Grubb, W. T. *Journal of the Electrochemical Society* **1959**, *106*, 275–278.
- (52) Luo, Z.; Chang, Z.; Zhang, Y.; Liu, Z.; Li, J. *International Journal of Hydrogen Energy* **2010**, *35*, 3120–3124.
- (53) Millet, P.; Dragoe, D.; Grigoriev, S.; Fateev, V.; Etievant, C. *International Journal of Hydrogen Energy* **2009**, *34*, 4974–4982.
- (54) Marangio, F.; Santarelli, M.; Call, M. *International Journal of Hydrogen Energy* **2009**, *34*, 1143–1158.
- (55) Millet, P.; Grigoriev, S. A.; Porembskiy, V. I. *Int. J. Energy Res.* **2012**, *37*, 449–456.
- (56) Wilson, M. S.; Gottesfeld, S. *J. Appl. Electrochem.* **1992**, *22*, 1-7.
- (57) Cho, J. H.; Kim, J. M.; Prabhuram, J.; Hwang, S. Y.; Ahn, D. J.; Ha, H. Y.; Kim, S.-K. *Journal of Power Sources* **2009**, *187*, 378–386.
- (58) Xie, J.; More, K. L.; Zawodzinski, T. A.; Smith, W. H. *Journal of the Electrochemical Society* **2004**, *151*, A1841.
- (59) Grigoriev, S. A.; Millet, P.; Volobuev, S. A.; Fateev, V. N. *International Journal of Hydrogen Energy* **2009**, *34*, 4968–4973.
- (60) Ahn, S. H.; Lee, B.-S.; Choi, I.; Yoo, S. J.; Kim, H.-J.; Cho, E.; Henkensmeier, D.; Nam, S. W.; Kim, S.-K.; Jang, J. H. “*Applied Catalysis B, Environmental*” **2014**, *154-155*, 197–205.
- (61) Park, S.; Shao, Y.; Liu, J.; Wang, Y. *Energy & Environmental Science* **2012**, *5*, 9331.
- (62) Greeley, J.; Markovic, N. M. *Energy & Environmental Science* **2012**, *5*, 9246.
- (63) Marshall, A.; Børresen, B.; Hagen, G.; Tsyppkin, M.; Tunold, R. *Energy* **2007**, *32*, 431–436.
- (64) Seley, D.; Ayers, K.; Parkinson, B. A. *ACS Comb. Sci.* **2013**, *15*, 82–89.
- (65) Smith, R. D. L.; Prevot, M. S.; Fagan, R. D.; Zhang, Z.; Sedach, P. A.; Siu, M. K. J.; Trudel, S.; Berlinguette, C. P. *Science* **2013**, *340*, 60–63.
- (66) Millet, P.; Ngameni, R.; Grigoriev, S. A.; Fateev, V. N. *International Journal of Hydrogen Energy* **2011**, *36*, 4156–4163.
- (67) Morales-Guio, C. G.; Hu, X. *Acc. Chem. Res.* **2014**, *47*, 2671–2681.
- (68) Ge, X.; Chen, L.; Zhang, L.; Wen, Y.; Hirata, A.; Chen, M. *Adv. Mater.* **2014**, *26*, 3100–3104.
- (69) Kanan, M. W.; Nocera, D. G. *Science* **2008**, *321*, 1072–1075.
- (70) Dincă, M.; Surendranath, Y.; Nocera, D. G. *Proceedings of the National Academy of Sciences* **2010**, *107*, 10337–10341.
- (71) Smith, R. D. L.; Prévot, M. S.; Fagan, R. D.; Trudel, S.; Berlinguette, C. P. *J. Am. Chem. Soc.* **2013**, *135*, 11580–11586.
- (72) Indra, A.; Menezes, P. W.; Sahraie, N. R.; Bergmann, A.; Das, C.; Tallarida, M.;



- Schmeißer, D.; Strasser, P.; Driess, M. *J. Am. Chem. Soc.* **2014**, *136*, 17530–17536.
- (73) Blakemore, J. D.; Schley, N. D.; Kushner-Lenhoff, M. N.; Winter, A. M.; D'Souza, F.; Crabtree, R. H.; Brudvig, G. W. *Inorg. Chem.* **2012**, *51*, 7749–7763.
- (74) Blakemore, J. D.; Schley, N. D.; Olack, G. W.; Incarvito, C. D.; Brudvig, G. W.; Crabtree, R. H. *Chemical Science* **2011**, *2*, 94–98.
- (75) Blakemore, J. D.; Mara, M. W.; Kushner-Lenhoff, M. N.; Schley, N. D.; Konezny, S. J.; Rivalta, I.; Negre, C. F. A.; Snoeberger, R. C.; Kokhan, O.; Huang, J.; Stickrath, A.; Tran, L. A.; Parr, M. L.; Chen, L. X.; Tiede, D. M.; Batista, V. S.; Crabtree, R. H.; Brudvig, G. W. *Inorg. Chem.* **2013**, *52*, 1860–1871.
- (76) Smith, R. D. L.; Sporinova, B.; Fagan, R. D.; Trudel, S.; Berlinguette, C. P. *Chem. Mater.* **2014**, *26*, 1654–1659.
- (77) Kuai, L.; Geng, J.; Chen, C.; Kan, E.; Liu, Y.; Wang, Q.; Geng, B. *Angew. Chem. Int. Ed.* **2014**, *53*, 7547–7551.
- (78) Pierson, J. F.; Wiederkehr, D.; Billard, A. *Thin Solid Films* **2005**, *478*, 196–205.
- (79) Slavcheva, E.; Radev, I.; Bliznakov, S.; Topalov, G.; Andreev, P.; Budevski, E. *Electrochimica Acta* **2007**, *52*, 3889–3894.
- (80) Rozain, C.; Mayousse, E.; Guillet, N.; Millet, P. “*Applied Catalysis B, Environmental*” **2016**, *182*, 153–160.
- (81) Millet, P.; Ranjbari, A.; de Guglielmo, F.; Grigoriev, S. A.; Auprêtre, F. *International Journal of Hydrogen Energy* **2012**, *37*, 17478–17487.
- (82) Grigoriev, S. A.; Dzhus, K. A.; Bessarabov, D. G.; Millet, P. *International Journal of Hydrogen Energy* **2014**, *39*, 20440–20446.
- (83) Reier, T.; Oezaslan, M.; Strasser, P. *ACS Catal.* **2012**, *2*, 1765–1772.
- (84) Oh, H.-S.; Nong, H. N.; Reier, T.; Glich, M.; Strasser, P. *Chemical Science* **2015**.
- (85) Antolini, E. *ACS Catal.* **2014**, *4*, 1426–1440.
- (86) Ayers, K. *II.A.8 Low-Noble-Metal-Content Catalysts/Electrodes for Hydrogen Production by Water Electrolysis*; DE-SC0008251; Department of Energy: Brookhaven, NY, 2013; pp. 1–4.
- (87) Millet, P.; Mbemba, N.; Grigoriev, S. A.; Fateev, V. N.; Aukauloo, A.; Etiévant, C. *International Journal of Hydrogen Energy* **2011**, *36*, 4134–4142.
- (88) Tang, H.; Wang, S.; Pan, M.; Jiang, S. P.; Ruan, Y. *Electrochimica Acta* **2007**, *52*, 3714–3718.
- (89) Lindermeir, A.; Rosenthal, G.; Kunz, U.; Hoffmann, U. *Journal of Power Sources* **2004**, *129*, 180–187.
- (90) Kadirov, M. K.; Bosnjakovic, A.; Schlick, S. *J. Phys. Chem. B* **2005**, *109*, 7664–7670.
- (91) Danilczuk, M.; Bosnjakovic, A.; Kadirov, M. K.; Schlick, S. *Journal of Power Sources* **2007**, *172*, 78–82.
- (92) Coates, J. In *Encyclopedia of Analytical Chemistry*; Meyers, R. A., Ed.; John Wiley & Sons Ltd.: Chichester, 2000; pp. 10815–10837.
- (93) De Almeida, S. H.; Kawano, Y. *Journal of Thermal Analysis and Calorimetry* **1999**.
- (94) Ito, H.; Maeda, T.; Nakano, A.; Takenaka, H. *International Journal of Hydrogen*

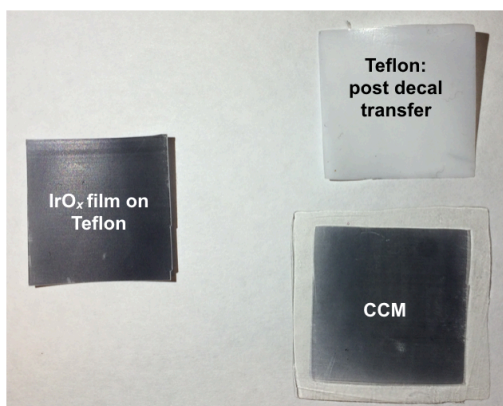
- Energy* **2011**, *36*, 10527–10540.
- (95) Soboleva, T.; Xie, Z.; Shi, Z.; Tsang, E.; Navessin, T.; Holdcroft, S. *Journal of Electroanalytical Chemistry* **2008**, *622*, 145–152.
- (96) Bard, A. J.; Faulkner, L. R. In *Electrochemical Methods: Fundamentals and Applications*; Swain, E., Ed.; John Wiley & Sons, INC.: New York, 2001; pp. 368–416.
- (97) Walter, M. G.; Warren, E. L.; McKone, J. R.; Boettcher, S. W.; Mi, Q.; Santori, E. A.; Lewis, N. S. *Chem. Rev.* **2010**, *110*, 6446–6473.
- (98) Cook, T. R.; Dogutan, D. K.; Reece, S. Y.; Surendranath, Y.; Teets, T. S.; Nocera, D. G. *Chem. Rev.* **2010**, *110*, 6474–6502.
- (99) Marini, S.; Salvi, P.; Nelli, P.; Pesenti, R.; Villa, M.; Berrettoni, M.; Zangari, G.; Kiros, Y. *Electrochimica Acta* **2012**, *82*, 384–391.
- (100) Vermeiren, P.; Moreels, J. P.; Claes, A.; Beckers, H. *International Journal of Hydrogen Energy* **2009**, *34*, 9305–9315.
- (101) Manolova, M.; Schoeberl, C.; Freudenberger, R.; Ellwein, C.; Kerres, J.; Stypka, S.; Oberschachtsiek, B. *International Journal of Hydrogen Energy* **2015**, *40*, 11362–11369.
- (102) Zhang, B.; Zheng, X.; Voznyy, O.; Comin, R.; Bajdich, M.; Garcia-Melchor, M.; Han, L.; Xu, J.; Liu, M.; Zheng, L.; Garcia de Arquer, F. P.; Dinh, C. T.; Fan, F.; Yuan, M.; Yassitepe, E.; Chen, N.; Regier, T.; Liu, P.; Li, Y.; De Luna, P.; Janmohamed, A.; Xin, H. L.; Yang, H.; Vojvodic, A.; Sargent, E. H. *Science* **2016**, *352*, 333–337.
- (103) Lewis, N. S. *Chem. Rev.* **2015**, *115*, 12631–12632.
- (104) Hunter, B. M.; Hieringer, W.; Winkler, J. R.; Gray, H. B.; Iler, A. M. M. X. *Energy & Environmental Science* **2016**, 1–10.
- (105) McCrory, C. C. L.; Jung, S.; Peters, J. C.; Jaramillo, T. F. *J. Am. Chem. Soc.* **2013**, *135*, 16977–16987.
- (106) Genovese, J. E.; Harg, K.; Paster, M.; Turner, J. A. *Current (2009) state-of-the-art hydrogen production cost estimate using water electrolysis*; Ruth, M.; Ramsden, T., Eds.; U.S. Department of Energy, 2009; pp. 1–51.
- (107) Chisholm, G.; Kitson, P. J.; Kirkaldy, N. D.; Bloor, L. G.; Cronin, L. *Energy & Environmental Science* **2014**, *7*, 3026–3032.
- (108) Daniel, L. Electrodeposition on non-conductive surfaces. US3865699.
- (109) Ambrosi, A.; Pumera, M. *Chem. Soc. Rev.* **2016**, 1–16.
- (110) Tan, Y. J.; Lim, K. Y. *Surface and Coatings Technology* **2003**, *167*, 255–262.
- (111) Smith, R. D. L.; Berlinguette, C. P. *J. Am. Chem. Soc.* **2016**, *138*, 1561–1567.
- (112) Trotochaud, L.; Ranney, J. K.; Williams, K. N.; Boettcher, S. W. *J. Am. Chem. Soc.* **2012**, *134*, 17253–17261.
- (113) Li, X.; Sabir, I. *International Journal of Hydrogen Energy* **2005**, *30*, 359–371.
- (114) Klaus, S.; Louie, M. W.; Trotochaud, L.; Bell, A. T. *J. Phys. Chem. C* **2015**, *119*, 18303–18316.
- (115) Louie, M. W.; Bell, A. T. *J. Am. Chem. Soc.* **2013**, *135*, 12329–12337.

- (116) Yeo, B. S.; Bell, A. T. *J. Phys. Chem. C* **2012**, *116*, 8394–8400.
- (117) Klaus, S.; Cai, Y.; Louie, M. W.; Trotochaud, L.; Bell, A. T. *J. Phys. Chem. C* **2015**, *119*, 7243–7254.
- (118) Nickel Institute. *Nickel Electroplating Handbook*; 2014; pp. 1–80.
- (119) Nie, J.; Chen, Y. *International Journal of Hydrogen Energy* **2010**, *35*, 3183–3197.
- (120) Wang, J.; Wang, H. *Fuel Cells* **2012**, *12*, 989–1003.

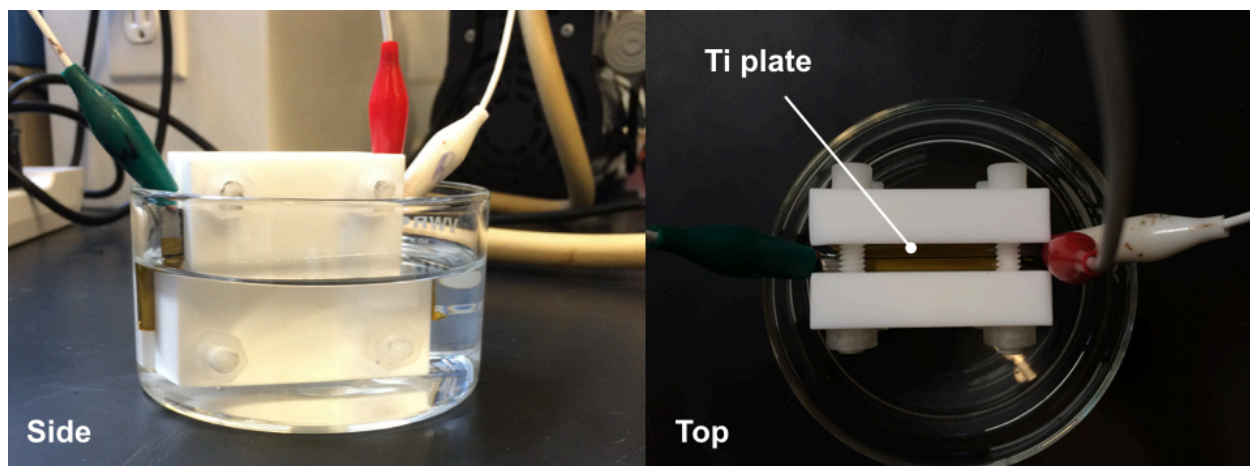
## Appendices

### Appendix A Supplemental photographs for Chapter 2.

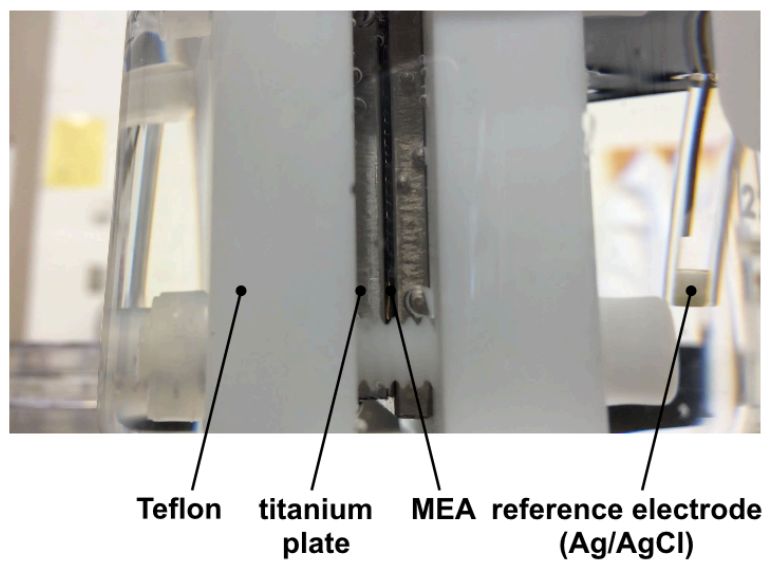
#### A.1 Teflon substrate before and after decal transfer.



#### A.2 Cell setup for electrochemical impedance studies on the through-plane ion conductivity of modified Nafion membranes

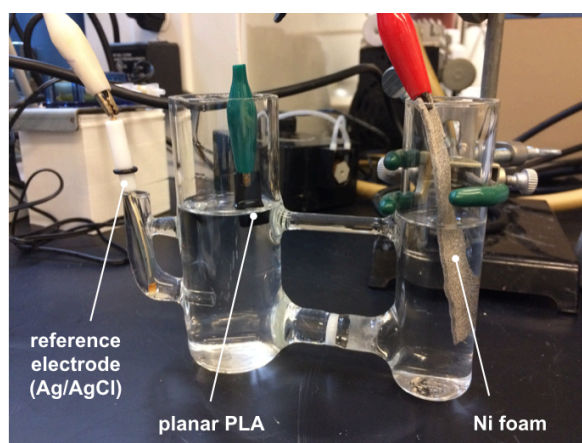


A.3 Cell setup for electrochemical experiments conducted on amorphous iridium coated membranes.



**Appendix B** Supplemental photographs for Chapter 3.

B.1 Cell setup for 3-electrode studies on 3D-printed planar electrodes.



## B.2 Plastic electrolyzer cell setup.

